Dual-Purpose Canister Filling Demonstration Project Progress Report

Spent Fuel and Waste Disposition

Prepared for

US Department of Energy

Spent Fuel and Waste Science and Technology

Nesrin O. Cetiner, Emilian Popov, Eliott J. Fountain, Venugopal K. Varma, Elvis Dominguez-Ontiveros, Abiodun I. Adeniyi, and Kaushik Banerjee

Oak Ridge National Laboratory

September 10, 2018

M4SF-18OR010305015/ M4SF-18OR010305015, Rev 1

ORNL/SPR-2018/973

This is a technical report that does not take into account the contractual limitations under the Standard Contract for Disposal of Spent Nuclear Fuel and/or High-Level Radioactive Waste (Standard Contract) (10 Code of Federal Regulations [CFR] Part 961). Under the provisions of the Standard Contract, the Department of Energy (DOE) does not consider spent nuclear fuel (SNF) in multi-assembly canisters to be an acceptable waste form, absent a mutually agreed to contract amendment. To the extent discussions or recommendations in this presentation conflict with the provisions of the Standard Contract, the Standard Contract provisions prevail.

ABSTRACT

This report discusses the initial progress made at the Oak Ridge National Laboratory to support direct disposal of dual-purpose canisters (DPCs) using filler materials to demonstrate that the probability of criticality in DPCs during disposal to be below the probability for inclusion in a repository performance assessment. In the initial phase of a multi-phase effort that will result in a full-scale demonstration, a computational fluid dynamics (CFD) model was developed to gauge the filling process and to uncover any unforeseen issues. The initial filling simulations of the lower region (mouse holes) of a prototypic DPC show successful removal of the inner space voids and smooth, even progression of the liquid level. In the initial phase, flow through a pipe that is similar to the drain pipe in a DPC will be investigated separately to gain valuable insight of flow regime inside a pipe. The initial experimental setups for validating the computational filling model have been designed, and the various assembly parts are being procured. The experience gained from the initial experiments will be applied to the next steps toward a full-scale demonstration and to the validation of multiphysics filling simulation models.

This page is intentionally left blank.

CONTENTS

This page is intentionally left blank.

LIST OF FIGURES

LIST OF TABLES

This page is intentionally left blank.

REVISION HISTORY

Revision	Changes Made
0	Initial issue
1	This revision incudes a description of a flow experiment through a pipe that is similar to the drain pipe in a DPC. This experiment will be used to gain insight into the flow regime inside a narrow, long pipe. All updates are identified by black vertical lines in the margin.

This page is intentionally left blank.

ACRONYMS

BWR	boiling water reactor
CCI	confocal chromatic imaging
CFD	computational fluid dynamics
DOE	US Department of Energy
DOE-NE	US Department of Energy Office of Nuclear Energy
DPC	dual-purpose canister
FCRD	Fuel Cycle Research and Development
FY	fiscal year
IFM	intermediate flow mixer
LDV	laser doppler velocimetry
NRC	Nuclear Regulatory Commission
ORNL	Oak Ridge National Laboratory
PDT	photochromic dye tracing
PIV	particle image velocimetry
PWR	pressurized water reactor
RTV	room temperature vulcanizing
SFP	spent fuel pool
SNF	spent nuclear fuel
UNF-ST&DARDS	Used Nuclear Fuel – Storage, Transportation & Disposal Analysis Resource and Data Systems
VOF	volume of fluid

This page is intentionally left blank.

DUAL-PURPOSE CANISTER FILLING DEMONSTRATION PROJECT PROGRESS REPORT

1. INTRODUCTION

This report documents work performed supporting the US Department of Energy (DOE) Nuclear Energy Spent Fuel and Waste Disposition, Spent Fuel and Waste Science and Technology, under work breakdown structure element 1.08.01.03.05, "Direct Disposal of Dual Purpose Canisters." In particular, this report fulfills the M4 milestone, M4SF-18OR010305015, "Summary status report of DPC filler demonstration project," as Revision 1 to M4SF-18OR010305017, "Unit test plan for filler demonstration," within work package SF-18OR01030501, "Direct Disposal of Dual Purpose Canisters–ORNL."

The commercial US nuclear utilities are currently storing spent nuclear fuel (SNF) onsite in spent fuel pools (SFPs) and dry storage systems. SFPs were initially constructed for temporary storage, but without SNF reprocessing options in the United States and with no final disposal pathway, SFPs started to reach capacity limits. Hence, to allow continued operation of the nation's commercial nuclear fleet, utilities started transferring SNF from SFPs (wet storage) to dry storage. As of June 4, 2018, there were 2,802 dry storage systems in use in the United States containing 117,737 spent fuel assemblies [1]. The majority of the dry storage systems currently being loaded are dual-purpose (storage and transportation) canister (DPCs). DPCs can accommodate up to 37 pressurized water reactor (PWR) assemblies and 89 boiling water reactor (BWR) assemblies, and they are designed primarily for storage and transportation. The DOE Office of Nuclear Energy (NE) is currently investigating the feasibility of direct disposal of DPCs in a geological repository to potentially offset the need to repackage currently loaded SNF into smaller disposal canisters. DPC direct disposal has many potential benefits, including cost savings in terms of billions of dollars, minimization of worker dose incurred from repackaging activities, and reduction of low-level radioactive waste in the form of discarded DPCs [2]. Although it has been indicated [2] that direct disposal of DPCs is feasible from a purely technical perspective, several engineering challenges, along with legal and policy issues, must be addressed to make DPC disposal a reality. One challenge is the potential for post-closure criticality in a repository time frame.

The potential for various DPC designs to achieve post-closure criticality configurations is under investigation using as-loaded DPC-specific criticality analysis. As-loaded criticality analyses of the currently loaded DPCs are being performed using the Used Nuclear Fuel-Storage, Transportation & Disposal Analysis Resource and Data System (UNF-ST&DARDS) [3] to evaluate uncredited margins that can be used to offset an increase in canister reactivity (calculated in terms of neutron multiplication factor, k_{eff}) due to various postulated degradation mechanisms in a repository time frame. Based on current modeling approaches [3], it has been shown that many of the loaded canisters have the potential to achieve criticality under the right conditions over a repository time frame (i.e., 10,000 years or longer) (Figure 1).

As shown in Figure 2, three approaches are under investigation to support post-closure criticality of DPCs in a repository time frame. The first approach is to perform detailed modeling and analysis of each loaded DPC; this effort is underway using UNF-ST&DARDS (Figure 1). The second approach includes a criticality consequence analysis to determine the impact of a potential criticality event on a repository performance assessment. The third approach is to investigate preconditioning of DPCs with engineering filler materials that can be credited over a repository time frame to displace the moderator material. (The introduction of a moderator material is needed to achieve in-canister criticality.) This report presents the progress made at Oak Ridge National laboratory (ORNL) to support adding a filler material to existing DPCs before placing them into a repository.

The work presented in this report focuses on initial evaluation of the filling option using simulations and prototypic (mockup) testing. The objective is to develop a DPC filling simulation that will be used to design a simple experiment of injecting surrogate filling materials through the drain pipe. The experimental data from the simple test will also be used to validate the simulation model. The objective of this simulation and simple test is to determine (1) whether a DPC can be filled using the drain pipe, (2) feasible filling rates, and (3) the volume fraction to be filled. Currently, two classes of engineering filling materials are under consideration: cementitious materials and low-temperature melting metals/alloys. The single physics flow simulation will be developed in phases, resulting in a fully validated multiphysics simulation to support and assess the DPC filling process. The multiphysics simulation will also be used to screen filler materials.

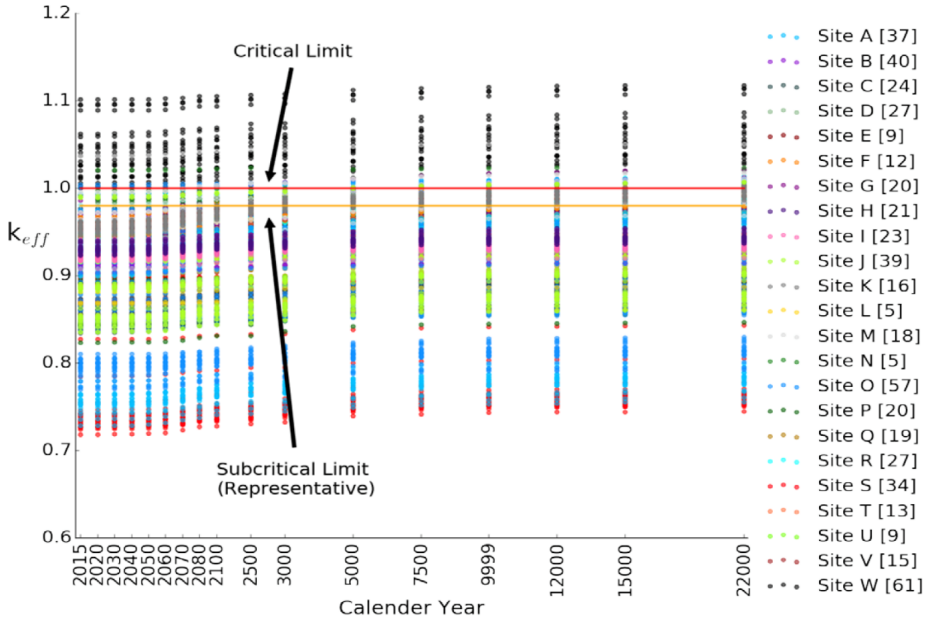

Figure 1. k_{eff} as a Function of the Calendar Year (up to Year 22,000) for 551 DPCs Loaded at 23 Sites. (Postulated degradation scenario includes loss of neutron absorber panels from basket over repository time frame.).

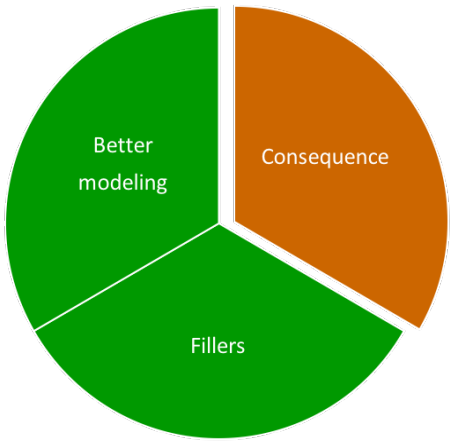

Figure 2. Three Components of a Long-Term DPC Disposition Evaluation Program.

This report is presented in two parts. The first part presents the progress made to develop a single physics filling simulation. The second part presents the progress made to develop an experimental setup to (1) validate the numerical simulation and (2) to understand various unforeseen issues of filling a DPC from the bottom. The objective is to understand various elements of the filling process and to gradually develop a fully validated simulation and test setup to present all the coupled processes involved in filling a canister with filler materials. This approach will identify a filling method (e.g., filling through the drain pipe, vent, or purpose-built access to the DPC's interior) that can be used with high confidence and to vet various potential filling materials as presented in "Joint Workplan on Filler Investigations for DPCs" [4].

2. FILLING SIMULATION

The objectives of the filling simulations are (1) to numerically analyze the filling process, initially on ideal surfaces, (2) to determine remaining voids and filling times, and (3) to identify potential problems. Simulations provide the flexibility needed to experiment with different liquids (metals) and surrogates, to explore filling methods based on existing or new canister features, to aid the experiment design by scaling major quantities.

A canister mockup test section is designed (Figure 3) and simulated. It represents the lower 16% of a real canister (height 74 cm, Ø26 cm), and it includes the passages among the assemblies' shrouds (mouse holes), the support stands (assembly spacer), the assembly's lower grids, and the first spacer grid. The design uses a 5 × 5 rod array, which is considered representative of a PWR fuel bundle. A circular container encloses five 5 × 5 bundles and accounts for most real canister features [5].

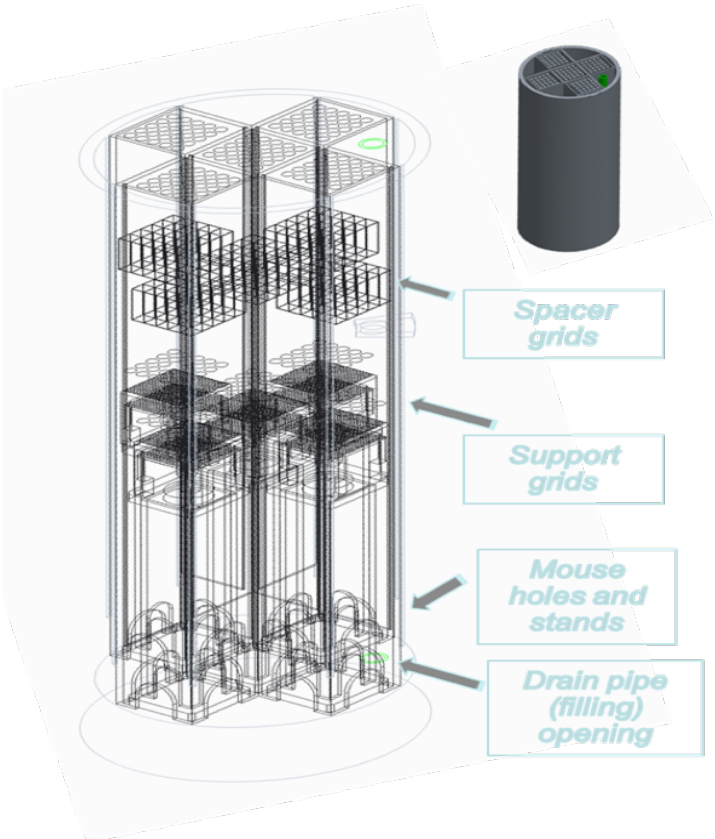

Figure 3. DPC Mockup (Based on 5 × 5 Bundles) of the Lower Section of the Real Canister, Including Mouse Holes, Supports, Lower Assembly Grid, and One Spacer Grid.

The simulation employs a 3-dimensional (3D) computational fluid dynamics (CFD) method for a two-phase two-component system in isothermal condition. The gas (helium) and the liquid (metals) front propagation is resolved by solving a viscous flow of mixture [6]. To implement this approach, the commercial software STAR-CCM+ is selected [7].

The problem is formulated within the framework of the segregated flow approach and discretized by the finite volume method. This includes and allows for coupling between the continuity and momentum equations. The following integral equations represent the conservation of mass and momentum (Navier-Stokes):

$$\text{Continuity: } \frac{\partial}{\partial t}\int_V \rho dV + \oint_A \rho \bar{V} \cdot da = 0\,, \tag{1}$$

$$\text{Momentum: } \frac{\partial}{\partial t}\int_V \rho \bar{V} dV + \oint_A \rho \bar{V} \otimes \bar{V} \cdot da = -\oint_A pI \cdot da + \oint_A T + \int_V f_g dV\,, \tag{2}$$

where V is volume, A is area, a is area vector, p is pressure, f_g is gravity force, ρ is density, $\bar{V}$ is velocity vector, T is stress tensor, and μ is dynamic viscosity. For laminar flows, the stress tensor is formulated as follows: $T = \mu[\nabla\bar{V} + \nabla\bar{V}^T - \frac{2}{3}(\nabla \cdot \bar{V})I]$, where I is the identity tensor.

To apply the flow model shown above to a filling problem that involves liquid and vapor phases, it is necessary to formulate it as a mixture. Mixture models are formulated using a Eulerian multiphase platform. Additional (phasic) quantities are introduced, all based on the volume fraction of one of the phases, *i*:

$$\rho = \sum_i \rho_i\,\alpha_i; \quad \mu = \sum_i \mu_i\,\alpha_i; \quad c_p = \sum_i \frac{(c_p)_i \rho_i}{\rho}\alpha_i; \;\; where: \; \alpha_i = \frac{V_i}{V} \;\; and \sum_i \alpha_i = 1. \tag{3}$$

Then a transport equation for the volume fraction is added to the system. The model is called *volume of fluid* (VOF) and has been proven to demonstrate accurate results with low computing cost.

$$\frac{\partial}{\partial t}\int_V \alpha_i dV + \oint_A \alpha_i \bar{V} \cdot da = \int_V \left(S_{\alpha_i} - \frac{\alpha_i}{\rho_i}\frac{D\rho_i}{Dt}\right) dV\,, \tag{4}$$

where S_{α_i} is the source of phase due to wall boiling, and $\frac{\alpha_i}{\rho_i}\frac{D\rho_i}{Dt}$ is the material derivative of phase density.

Two types of materials are considered as filler candidates. ORNL is investigating low melting temperature metals and surrogate liquids, and Sandia National Laboratory is studying the use of slurries

(concrete mixtures). An initial list of fillers used in numerical simulations is given in Table 1. Note that these are not necessarily candidates for final application but are mainly for numerical simulation in the simple unit test for validation. Two transport properties are important for this phase of the filling evaluation: density and dynamic viscosity. Silicone oils are highly ranked candidates due to their low cost and the large available selection of viscosities.

One half (central symmetry) of the geometry in Figure 3 is initially considered. It has a volume of 11.46 liters Figure 4). With a scaling factor to the real geometry of about 6.5, and with an estimate of 17 hours for filling time of the real canister, the filling rate for the model is determined to be 1.26 cm^3/s. Note that this is true for one half of the geometry. For testing, the filling rate of the entire volume must be two times higher. The Reynolds numbers (Re) for such filling rates and length scales, which are typical for rod bundles, are in single digits at Re~3, which justifies the laminar flow regime assumption. The entire geometry was modeled initially, resulting in a computational grid consisting of about 6M elements. The liquid is fed through the inlet section of the drain pipe, as shown in Figure 4. A velocity boundary condition is defined at the drain pipe orifice (area 180 mm^2) with a velocity magnitude of 1.26/180 = 0.007 m/s. Thus, the filling simulation is separated from the drain pipe simulation. The flow regime in the vertical drain pipe is subject to separate evaluation, which is currently under investigation. The formulation of that study is provided below.

Table 1. Preliminary list of liquids for testing and filling simulations.

Material	Melting Temp. (°C)	Density (g/cm^3)	Viscosity (Pa·s)	Reference
Glycerin ($C_3H_8O_3$)	Liquid	1.26@RT	0.95@RT	www.MatWeb.com
Silicon oil	Liquid	0.96@25C	0.33@25C	www.sigmaaldrich.com
Lead	327 (600K)	10.70 @600K	0.0026@600K	V. Sobolev (2007)
Lead-bismuth	124 (398K)	10.53 @398K	0.0032@398K	B. Alchagirov (2003)
Mercury	Liquid	13.53@RT	0.0015@RT	Thermal Fluids Central
Water	Liquid	9.97@RT	0.00088@RT	Web (for comparison)

Calculations are run in parallel on 32–640 computing processors. To properly capture the liquid level progression, the time step must be kept between 1–5 ms. The shortest runtime during this preliminary phase was 0.7 hour for one second of the filling process. Filling the entire geometry would take days of computing, so the strategy was changed. The major objective of a filling simulation is to predict the level progression and the void removal. Both of these occur near the current level position. The areas of computational domain below and above the level have little-to-no influence on the filling, but they consume computing resources. To reduce the computing burden, the domain is decomposed into smaller regions, and a data mapping algorithm is applied. The regions overlap, and the velocity and the void fraction (liquid) are mapped from one region to another. The canister geometry further facilitates this approach because the area above the mouse holes is composed of parallel channels (bundle region), and only one channel can be modeled. This radically reduces the computing load.

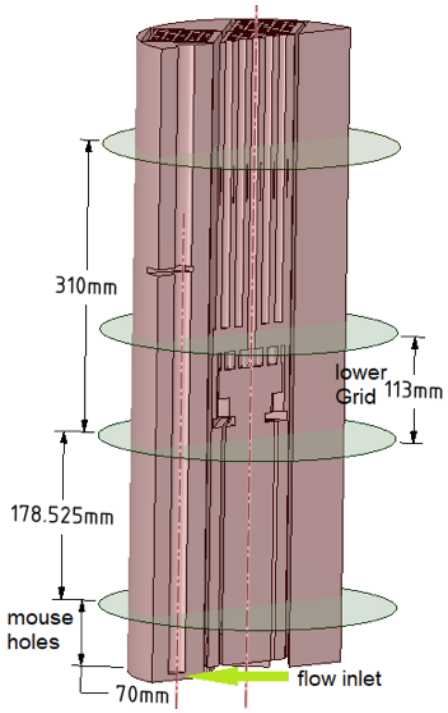

Figure 4. Model Split, Indicating the Sections of the Geometry Modeled.

2.1 Filling of the Mouse Hole Region

First the mouse hole region is separated and modeled, as shown in Figure 4. The overall height of the section shown is 70 mm, and it comprises the entire geometry. A polyhedral grid of about 45,000 elements was used. The wall mesh is displayed in Figure 6. It gives a perspective of the geometry with a clear view of the mouse holes. The objective of this simulation is to demonstrate that the mouse holes can be successfully filled if the drain pipe opening provides a continuous constant flow of 1.26 cc/s. The runs are performed on 32 processors for ~5 days (average runtime is 0.12 hour/sec of transient) with a time step of 5 ms. Simulations of the following liquids have demonstrated successful filling of voids in the mouse holes region: glycerin, lead-bismuth, silicone oil, and mercury. Mercury (Hg) is not an option for a real application, but due to its low viscosity and high density, it represents a bounding scenario for the simulation. No noticeable level deformations are observed when different liquids are used. The filling rate is low enough to avoid any local effects that could compromise the filling. This is illustrated in Figure 5. , which plots sections of the mouse hole region for two liquids: lead-bismuth (Pb-Bi) and silicone oil. Even though the densities of these liquids differ by about ten times and the viscosities differ by about hundred times, the filling looks the same. The plot in Figure 5. shows the liquid level at 400 s and at the end of the filling process (total time 1020 s), when the level is at the middle and at the top of the mouse holes. No visible differences are noticeable. The volumes of injected liquids are the same: 496.5 cc for silicone oil, and 498.2 cc for Pb-Bi at 400 s. The small differences are due to computational inaccuracies because the filling rate is the same for both liquids.

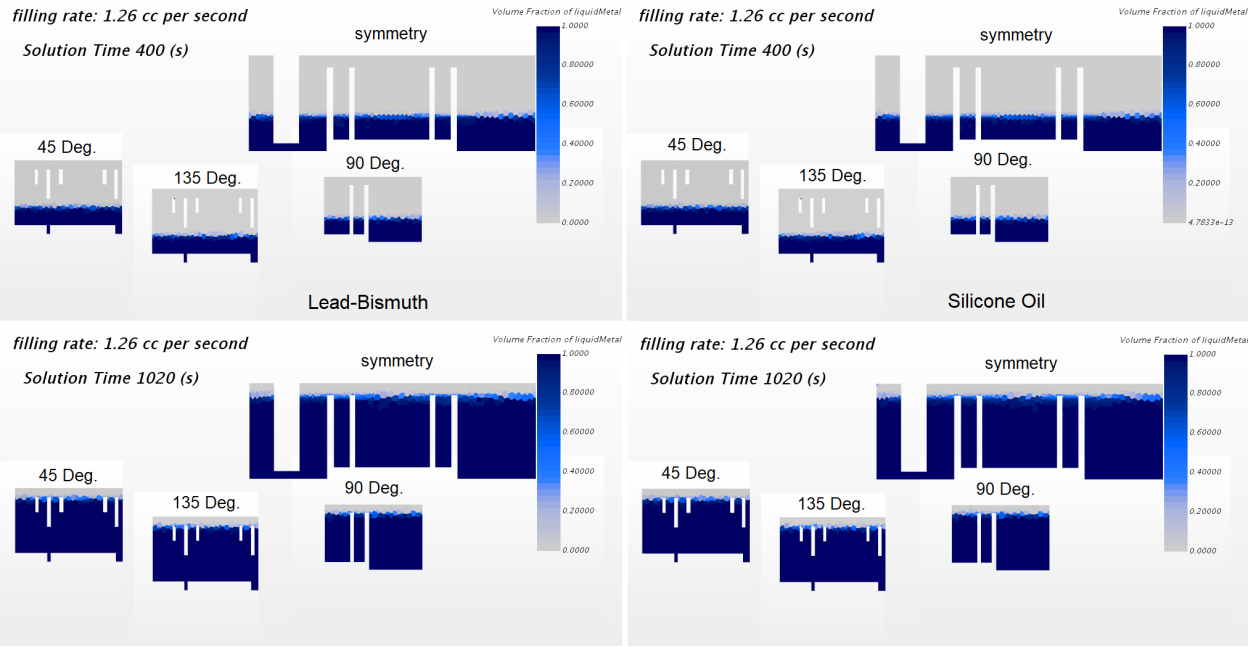

Figure 5. Liquid Levels at 400 and 1,020 s (end) of Transient from Two Runs with Different Liquids (Left: Lead-Bismuth; Right: Silicone Oil), and Contours of Levels at Several Sections of the Mouse Hole Region (Symmetry, 45-, 90-, and 135-Degree Cross Planes).

Even though the silicone oil density is much lower, it allows for the liquid to level off and to smoothly cover the entire region. The level velocity of 4.2 mm/min is such that the viscosity/density combination of the liquids does not affect the filling process. A detailed examination of the plotted sections does not show the presence of any voids. The same is confirmed by the overall volume balance, which is controlled during the simulation.

An isometric view of the simulated section is shown in Figure 6. The top wall and the symmetry planes are removed for better visibility inside the domain. The top part, as seen in Figure 5. , is added to the model to make the outlet pressure equal for all parallel cells. The DPC is designed so that each individual fuel bundle is confined in a separate shroud (cell). The cell walls do not allow for cross flow in the canister. The parallel cells are formed just above the mouse hole region, and the mouse holes are the only flow passage that permits the liquid to enter the fuel bundle cells. In order to properly simulate the filling of these individual cells, an extra volume is artificially added on top of this section to connect the parallel cells. This volume is not filled and does not affect the overall filling time or mass balance.

The views in Figure 6. provide another look at the filling process in the mouse hole region of the canister. This is the region where the bundle shrouds interconnect. The view on the left in Figure 6. shows an early stage of filling in which the central part is still not flooded. The liquid initially propagates on the circumference around the outside wall before entering the central area. Even though that space is narrow, the liquid can freely penetrate the space and distribute evenly in the remainder of the domain. The right view in Figure 6. shows a later stage of the filling in which the mouse holes are partially filled. By observing the levels in different cells, one can conclude that the process is very smooth, and the level rises evenly in all cells. Although the resolution of the model is quite low (to keep the compute time short), the numerical scheme used (high resolution level tracking) maintains the level within 1–2 grid elements. No numerical diffusion is observed due to the second order upwind scheme used to run the simulations. Note that the interface between the gas and liquid cannot be sharper than one element (the liquid boundary to match the element boundary) because the VOF method treats the liquid as a fraction of the total fluid, and as soon the level crosses the element boundary, the void fraction in the same element starts to increase

and varies from 0–1 before the element is completely filled. This explains the different color of gradient in the elements near the level.

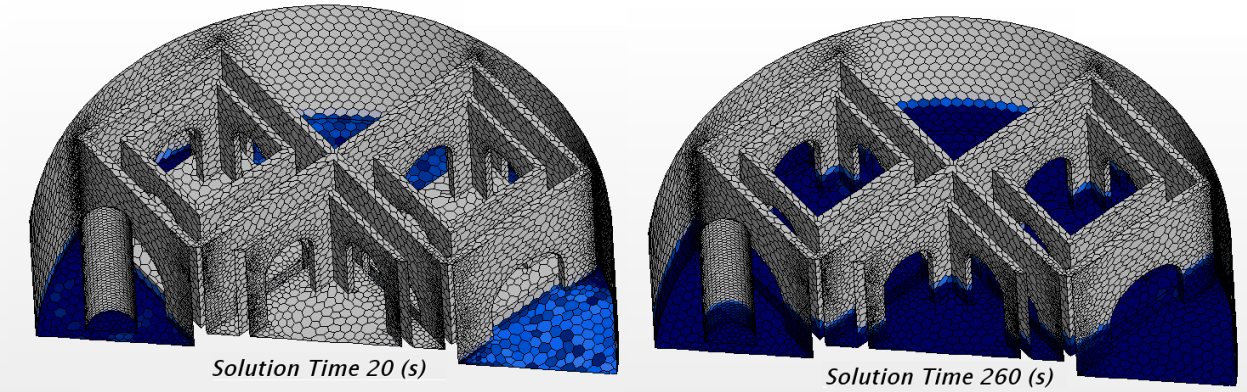

Figure 6. Liquid Content during Filling of the Mouse Hole Region at 20 and 260 s. Total Filling Time = 1,040 s; the Computational Grid is Also Shown.

An important aspect of the filling calculations is the conservativeness of the solution. The relatively coarse domain discretization poses questions about the solution's accuracy. To address these questions, a control of the mass in the system is established during the time advancement. The result is plotted in Figure 7. for three of the test liquids (Pb-Bi, Si-oil, Hg), and it shows that the error varies within 1.5%. In the simulation, the model fills for 1,040 s while the actual filling time is 1,024 s. The error tends to increase toward the second half of the process, which will be investigated in the future. The error could be due to the grid becoming larger in the space over the mouse holes. Usually, the element size is driven by the geometry features, and to resolve small details, more elements are used. Once details such as the mouse holes are meshed, the grid elements become larger in the spaces over the mouse holes. This may be increasing the error, but it remains within practical limits. In view of the long practical filling times, such a small difference is considered acceptable.

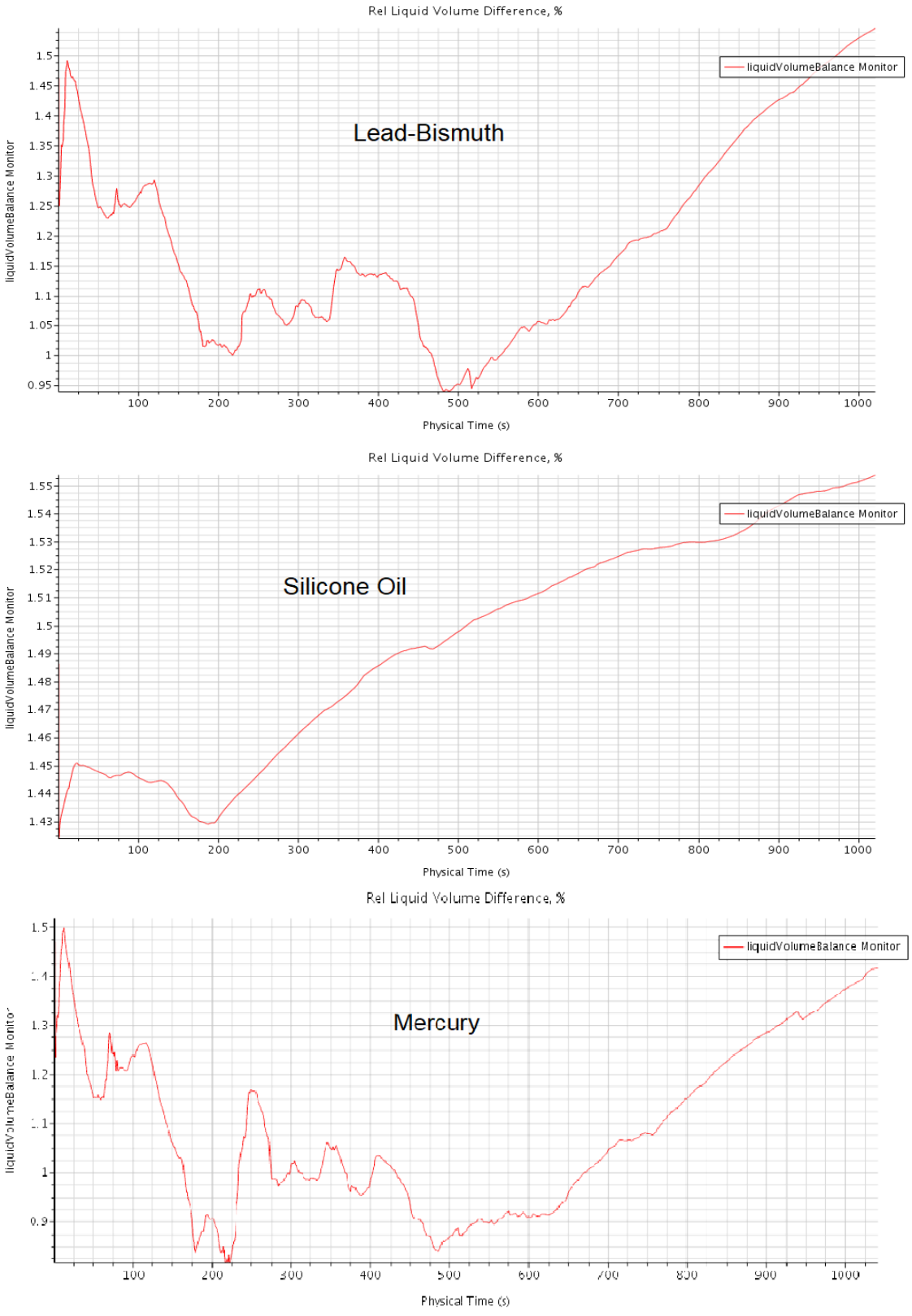

Figure 7. Mass Error Evolution during Filling of the Mouse Holes Region with Pb-Bi (Left), Silicone Oil (Center), and Mercury (Right).

2.2 Lower Grid Filling Simulation (In Progress)

As shown in Figure 4, upstream of the mouse holes, there is a section (~180 mm) where the geometry does not change. This section contains the liquid in the fuel assemblies' supports. The fuel assemblies are placed in the canister on rectangular supports that separate them from the canister floor. After filling of the mouse holes has been successfully demonstrated, there is no need to carry the numerical solution in that region because no new geometry features exist. Instead, this section is skipped by shortening the domain to save computing time. The level, which is computed in the region below (mouse holes), is transposed as an input condition, assuming it has the same topology. The rationale is based on the fact that no specific features of the level are observed, like moving or standing waves, substantial radial convection, etc., which would invalidate the above assumption. The liquid front propagates in all cells with the same velocity. Technically, this is accomplished by mapping data between nonconformal domains, which is challenging in CFD computing, but it can be done. This approach is followed in the present analyses.

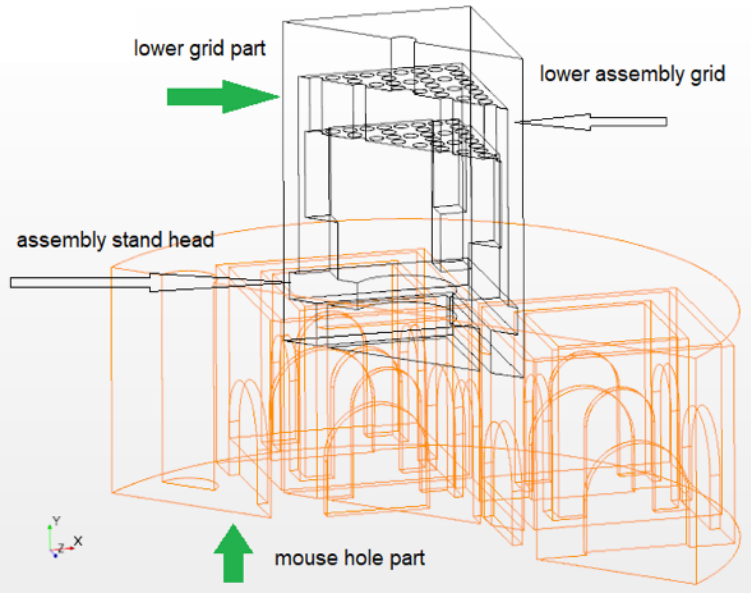

Figure 8. Lower Grid and Its Relative Position to the Mouse Hole Region Used in the Simulation. The Important Features of That Section Are Indicated.

The simulated section is shown in Figure 4 and is labeled *lower grid* because the most representative feature of that region is the lower fuel bundle grid. This grid includes several small holes that, in the reactor design, were originally meant to provide more even flow distribution at the bundle's inlet. These holes may pose a problem in the filling process and will require special attention. The modeled section also includes the upper part of the assembly stand and the transition region. It is part of one of the five 5 × 5 bundles. As mentioned before, the bundle cells (shrouds) permit the domain to be further decomposed and simplified by simulating only one of the five bundles (because they form identical parallel channels).

More detail about these components and their relative positioning is shown in Figure 8. The mouse hole region is shown with different colors to distinguish the components. The section has an overall height of 113 mm. It is set to overlap the mouse hole region, with 15 mm to allow for data mapping. The overlap is shown in Figure 8. The lower grid section is meshed with about 100,000 elements. When compared to the mouse hole region, this increased number of elements is about 5 times larger and has 45,000 elements. This is caused by the holes in the lower assembly grid.

To provide continuity of the filling process, two variables from an existing solution in the mouse hole region must be mapped to the lower grid region. One of them is the current level, expressed as liquid volumetric content (fraction of total fluid). The level is usually spread across at least three layers of elements, which determines the mapped domain. Figure 9 (below) shows the outcome after the mapping is performed. A partial level of data only in the central cell is mapped to the lower grid region. It covers part of the bundle support fluid volume just below the lower grid. The volume of this initial liquid is 15 cc, and it must be accounted for in the over-volume balance during the simulation. The computational mesh is demonstrated in Figure 9. (below), with a zoom into the lower grid holes. The geometry is captured in full detail, resulting in an increased element count.

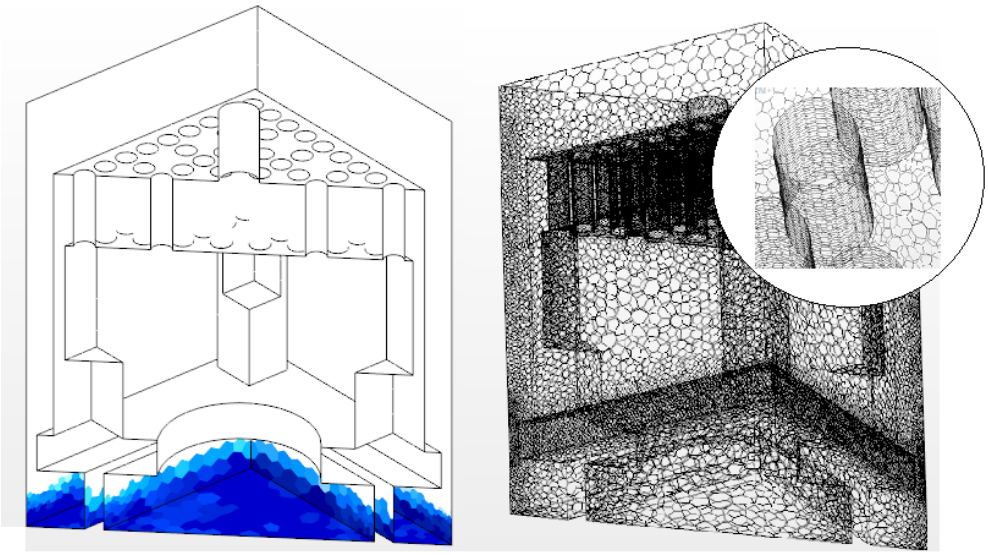

Figure 9. Initial Liquid Fraction as Mapped from the Mouse Hole Region (Left), and Computational Mesh of the Lower Grid Region with a Zoom into the Hole Area's Mesh (Right).

The second variable that must be transferred from the previous solution is the velocity vector at the inlet of the new section. A close examination of velocity vectors in a plane just above the mouse holes (Figure 10.) shows a random high frequency distribution of instantaneous velocities. The dominant magnitude is around 0.05 m/s, with no preferential direction. The insert window in Figure 10. enlarges the velocities in the mapped area and shows the computational grid. Such a velocity profile is calculated by the viscous solution when no ensemble time averaging of velocity is performed. The difference between the instantaneous velocity and the axial average velocity (~4mm/min) indicates that a small-scale turbulence is computed in a general laminar flow. Further examination of the velocity contours in the mouse hole region does not indicate formation of eddies, indicating that the flow is not turbulent. The Re numbers for that region, based on the level velocity and typical length scales (~70mm), are ~15. This finding requires more attention and further analysis of the origin of these fluctuations, which are most likely numeric.

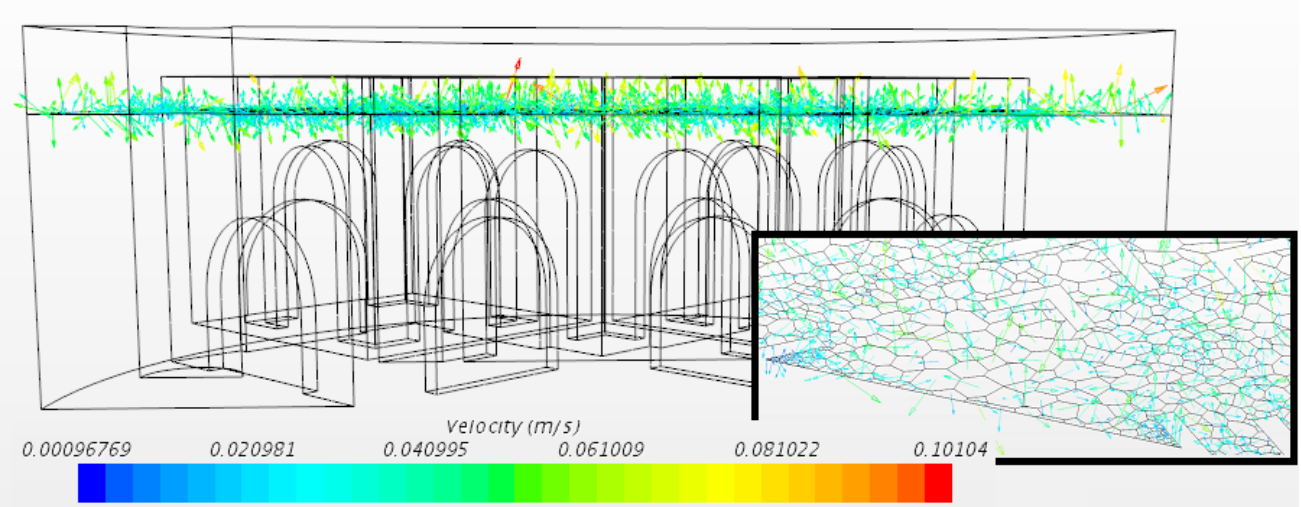

Figure 10. Velocity Vectors of the Advancing Liquid Level on a Plane Just above the Mouse Holes. The Random Fluctuation of Liquid is Noticeable, with no Preferential Direction. The Insert Shows the Mesh and the Velocities in the Mapped Region.

Based on the results discussed above, instantaneous velocities are not suitable as a boundary condition for the lower grid region unless they are time averaged. Instead of time averaging, the velocity at the inlet section of the lower grid region is calculated after the filling rate for the same region is calculated. Additional data are needed to perform this calculation, as summarized in Table 2.

Table 2. Geometry data for the lower grid section and for the entire geometry with the same axial elevations.

Parameter	Value
Volume of lower grid region	224 cubic centimeters (cc)
Axial height of lower grid region	113 mm
Inlet flow are of lower grid region	2137 mm^2
Local volume of entire geometry (113 mm)	2047.8 cc
Overall filling rate for the entire model	1.26 cc/s

The approach is based on calculating the overall time for filling a section of the entire geometry with the same axial marks as the lower grid section: 113 mm. The filling time of the entire geometry with 113 mm height = volume (local) of entire geometry / overall filling rate:

$$T_{total} = 2047.8/1.26 = 1625 \text{ s} \quad (5)$$

If the same filling time is valid for the lower grid section of the geometry, then a part specific filling rate can be calculated:

$$\text{Filling rate (lower grid)} = \text{volume of lower grid} / T_{total} = 224 / 1625 = 0.138 \text{ cc/s} \quad (6)$$

Once the part-specific filling rate is known, the inlet velocity is calculated:

$$\text{Inlet velocity for the lower grid section} = \text{Filling rate (lower grid)} / \text{inlet flow area} = 0.138 / 2137 = 6.45\text{E-}5 \text{ m/s} \quad (7)$$

This velocity is slightly lower than the level advancement velocity of 4.2 mm/min (7.0E-5 m/s) mentioned before. The difference appears because the flow area in the lower grid section is smaller than the average flow area in the same section of the entire geometry. The inlet velocity is applied to the inlet geometry of the lower grid section together with mapping the level from the mouse hole section. These

two initial conditions are sufficient to perform the calculations. The mapping is successfully accomplished following a code-specific procedure, and the analyses runs will be initiated soon.

The computational runs are successfully started and are under way at the time of this writing. They are being executed on 96 cores (three nodes 32 cores each). The first 500 s of the transient are calculated. The level progresses smoothly as in the previous DPC section (mouse holes) without any anomalies. The liquid level has not reached the lower grid area and it is still in the transitional region between the assembly stands/spacers and the lower grid. Four snapshots of the entire lower grid section showing the level advancement are plotted in Figure 11. The grid hole area is clearly visible above the current level position.

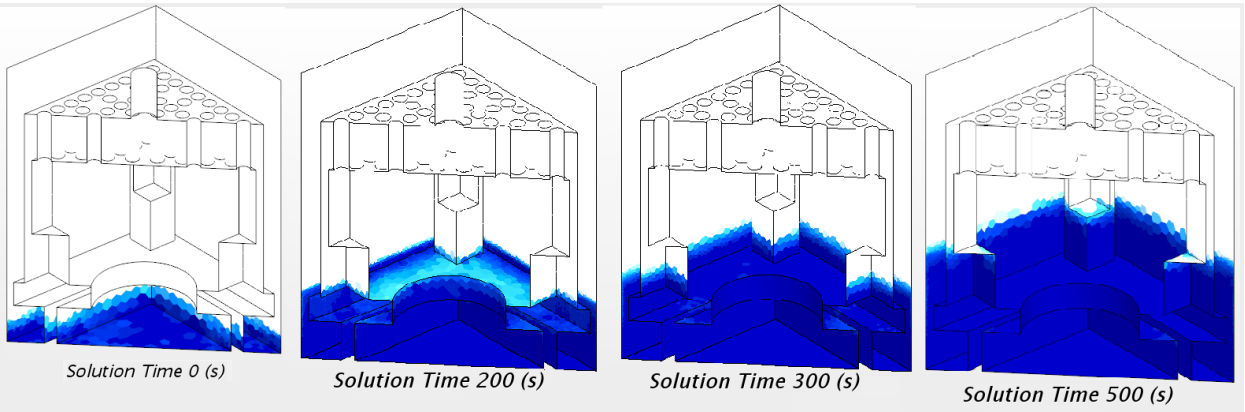

Figure 11. Evolution of the Level in the Lower Grid Section of the Model during the First 500 s of Transient.

In terms of resolution, the holes are the denser part of the domain and will require more computing time. The period of 500 s is computed for about 19 hours of CPU time per processor, or with about 0.2 hour of clock time per second of real process. At this speed, the entire filling simulation should be completed within a week.

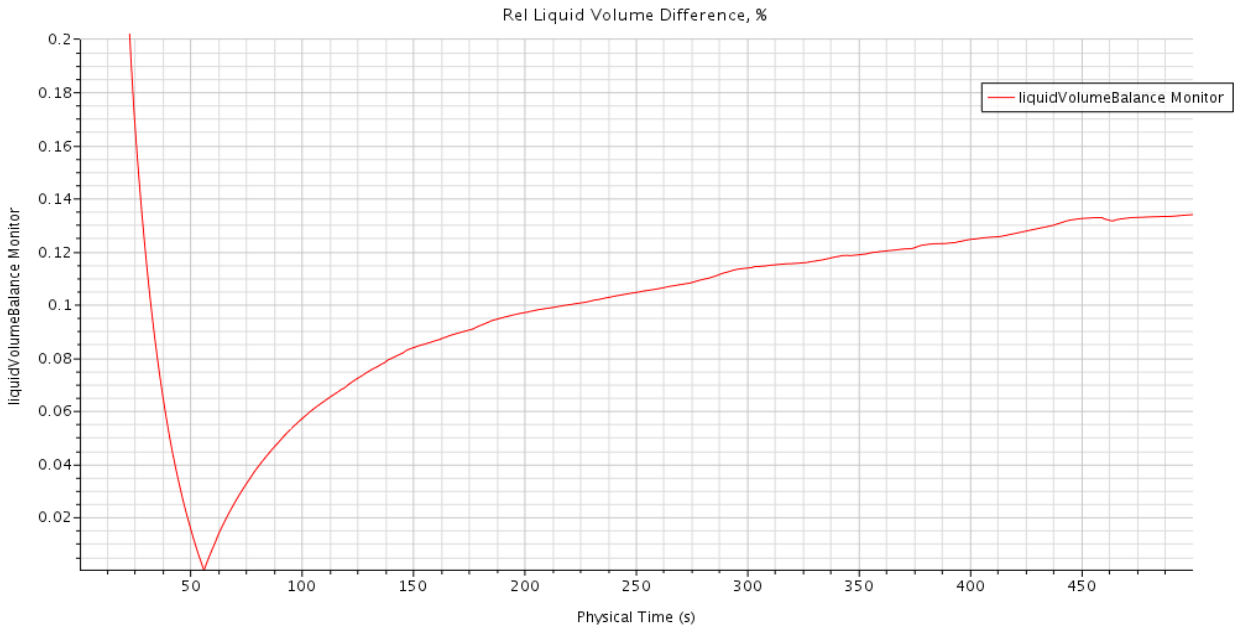

Figure 12. Mass Error Monitor. The Total Mass in the System is Constantly Evaluated and Compared to an Ideal Process.

The mass error is continuously being monitored (Figure 12). The current value is about 0.14%, which when converted to real volume yields 0.3 cm^3; it tends to stabilize at this level. This number indicates a very good solution convergence and accurate spatial discretization.

To allow for axial tracking of the filing process and identification of eventual voids, several cross sections of the domain are plotted in Figure 13. They are taken in the symmetry plane (mid-section) and at 45, 90, and 135 degrees sections. The information from these plots shows an even level progression and no void formation. The most critical area for voids is the grid, and the solution has not yet reached that location. The section that has already been filled is quite free of obstruction, as the flow enters by a central opening with a large area which does not present a challenge.

The simulations continue, and without any further complications, they are expected to complete in a week, depending on the load on the computing cluster.

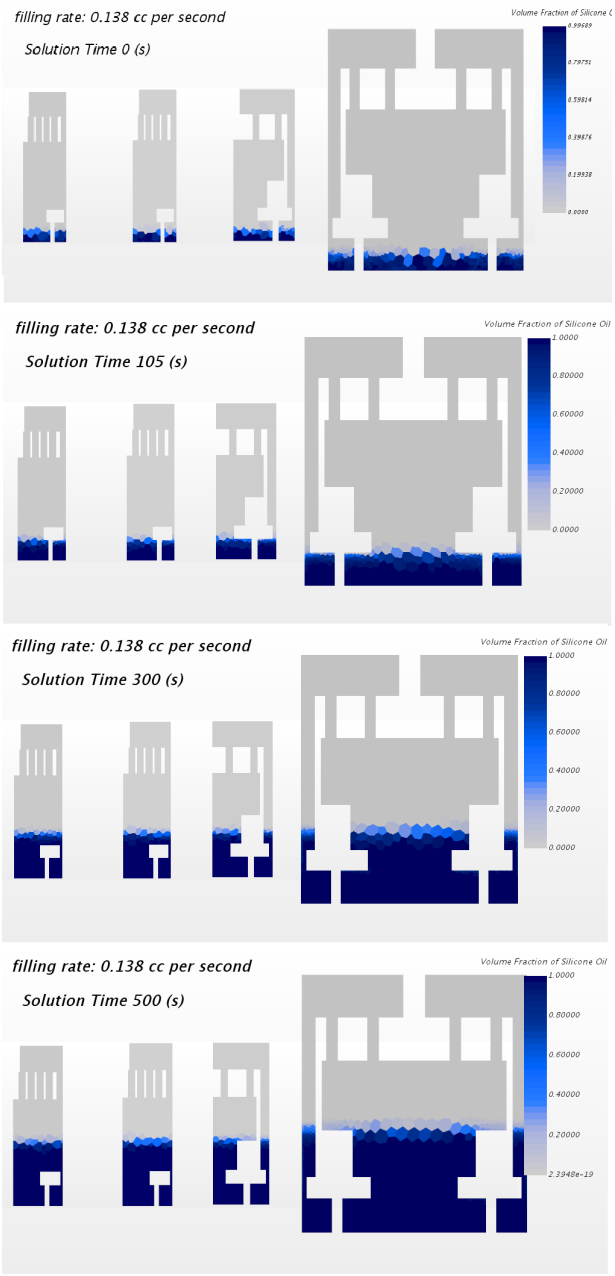

Figure 13. Filling of Lower Grid Region, Sectional Liquid Fraction Plots, Showing the Volume of the Lower Grid Filled at Different Time Instances. The Calculated Period Covers the Transition between the Stand and the Grid Entrance Region.

2.3 Drain Pipe Analysis and Modeling Approach (Not Started Yet)

The drain pipe analysis and modeling evaluations have not been initiated yet because the filling simulations are receiving higher priority. The information presented here is preliminary should be considered an introduction to the problem.

One consideration is to evaluate the possibility of filling the canister through the drain pipe. Each DPC is equipped with a drain pipe and a vent port of the same size (ID 1.25 in.). The drain pipe stretches from the top of the canister to the bottom, so it has the same length as the canister. The pipe is about 4.26 m (14 ft.)

long. While there is no strict requirement for how much time the filling of a single canister should take, the drain pipe's capacity to deliver a steady flow of liquid metal to the canister may be the limiting factor for the filling time and could be the component that will define this time. In the simulations, a filling time of 17 hours is assumed based on a filling rate of 100 ml/s. The assumed free canister volume is 6 m^3.

Extensive research has been conducted on flows in vertical pipes. In the past, intrusive methods such as hot wire anemometry were used, but more recent experimental works use non-intrusive techniques such as laser doppler velocimetry (LDV), photochromic dye tracing (PDT), confocal chromatic imaging (CCI), or particle image velocimetry (PIV). Two recent experimental and theoretical studies by Zadrazil and Markides [8] and by Padmanaban [9] address vertical pipe flows, mainly of water. When the pipe entrance is not obstructed by liquid (as in a pipe draining a tank) but is left open to the air or a gas atmosphere, the flow that develops in the pipe is a two-phase annular flow. In this type of flow, the liquid flows steadily on the pipe walls, forming an annular film. The core of the flow is gaseous and is typically stagnant. Some experiments consider co- or counter-current gas flows [9], but they are outside the initial scope of this work. Co- or counter-current gas flows are of interest for the canister filling because they would provide a means to control the flow rate without chocking the pipe. The term *chocking* is used here to indicate a regime in which the entire pipe area can become fluidized, and there would be no free flow of gas in the pipe. These evaluations will initially be assumed that this type of regime is unwanted, as it would impede the steadiness of canister filling by creating flow pulses, shocks (hydro) or other hydraulic phenomena. This could damage canister structures or disrupt the filling process due to the high gravity effect of liquid metals, which have densities approximately 10 times greater than that of water. This option will be further reevaluated during this study and may be revised. Figure 11 presents a typical drain port design.

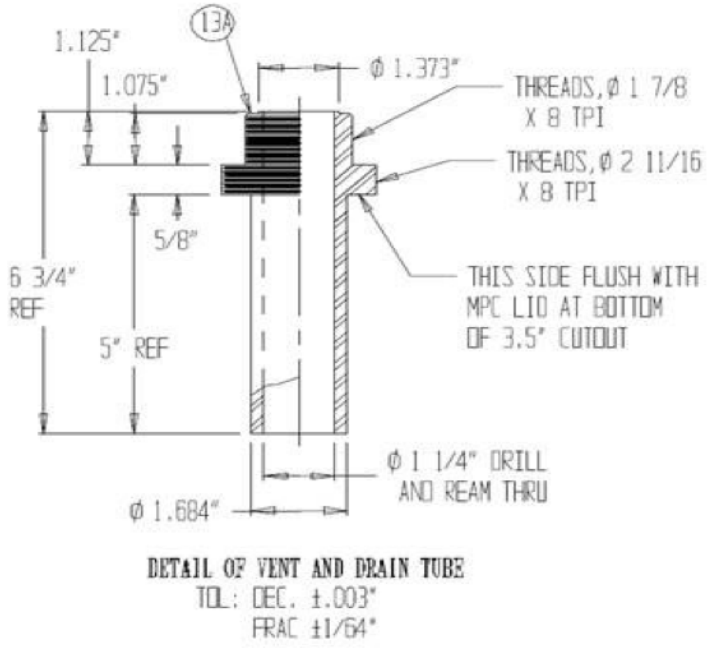

Figure 14. Drawing of the Drain Port Showing the Side of the Opening [5].

The Nusselt film theory can be used as a starting point in these analyses because it gives a good first order approximation to the main flow characteristics. It is based on the assumption that a steady liquid film forms on the pipe inner wall (or other structure wall) which is one dimensional (only in axial direction) and the film flow is laminar. Under such circumstances, the wall shear stress balances (in a steady condition, when the axial velocity is constant) with the force of gravity. This can be written as

$\frac{\partial \tau_{yz}}{\partial y} = -\rho g$, where τ is the shear stress in z (axial) and y (normal to the wall) direction; g is gravity; and ρ is the liquid density. Normally, the z-y shear component can be presented as $\tau_{yz} = \mu(\frac{\partial W}{\partial y} + \frac{\partial V}{\partial z})$, with the second term in one dimensional flow is given by $\frac{\partial V}{\partial z} = 0$. Thus, the final equation that defines the film velocity becomes:

$$\mu \frac{d}{dy}\left(\frac{dW}{dy}\right) = -\rho g, \tag{8}$$

where W is the axial and V is the radial velocity component. In one dimensional formulation, only W is non- zero. The above equation can be integrated with the following boundary conditions: W =0 at the wall, and $\frac{\partial W}{\partial y} = 0$ at the film thickness of y = δ. The result gives the velocity distribution in the film:

$$W(y) = \frac{g}{\nu}\left(\delta . y - \frac{y^2}{2}\right), \tag{9}$$

where ν is the liquid kinematic viscosity and δ is the film thickness.

Assuming further a flat film (not exactly the same that forms in a circular pipe), the flow rate of liquid per unit width of film can be calculated by integrating the following expression over the film thickness:

$$q = \int_0^{\delta} w(y)dy . \tag{10}$$

The result of the above integration provides a simple relation between the film thickness and the volumetric flow rate:

$$\delta = \left(\frac{3\nu q}{g}\right)^{\frac{1}{3}}. \tag{11}$$

This relation can be used as a first approximation for evaluating the film thickness that forms in laminar conditions in a gravity driven flow. To make that relationship applicable when the flow rate Q (m^3/s) is known, an additional assumption for the film width is necessary. In case of very thin films, the film width of a film flowing on the inner pipe wall, will be very close to the pipe perimeter. In such condition, the relation between Q and q is given by: $q = Q/\pi D$, (m^2/s), where D – is the pipe diameter.

With the help of the above relation the film thickness can be finally evaluated as:

$$\delta = \left(\frac{3\nu Q}{\pi g D}\right)^{\frac{1}{3}}. \tag{12}$$

The non-dimensional parameter that characterizes the flow of liquid films is the Reynolds number *(Re)*. Traditionally in the liquid film flow theory, the *Re* number is defined in two different ways: by the Nusselt velocity W_{Nu}, or by the superficial velocity W_{sl}. The Nusselt velocity is formulated directly from the flow rate defined above:

$$W_{Nu} = \frac{q}{\delta} = \frac{\frac{g}{\nu}\delta^2}{3}. \tag{13}$$

The definition of the *Re* number is based on the Nusselt velocity and the film thickness and is given by:

$$Re_{Nu} = \frac{W_{Nu}\delta}{\nu} = \frac{g\delta^3}{3\nu^2}. \tag{14}$$

The formula allows the film thickness to be calculated by knowing the Nusselt Reynolds number.

Substituting the film thickness in the above, leads to a relatively simple relation between the *Re* number and the flow rate:

$$Re_{Nu} = \frac{q}{\nu} = \frac{Q}{\pi \nu D}. \quad (15)$$

For Lead-Bismuth (Pb-Bi) eutectic (ν = *3.039E-7* m^2/s) and for the chosen flow rate of *100 ml/s (Q = 1.0E-4* m^3/s*)*, and for the size of the drain line *(ID = 1.25" = 0.03175 m)*, the Nusselt Re number is: Re_{Nu} *= 3298*. The Nusselt film thickness can also be calculated, using the above formulas for Pb-Bi: δ *= (3.3.039E-7.1.0E-4/π/9.81/3.175E-2)^1/3 = 0.45 mm*. The corresponding Nusselt velocity can be used as a measure of some average film velocity. It is formulated above and is calculated below:

$$W_{Nu} = \frac{q}{\delta} = \frac{Q}{\pi D \delta} = \frac{1.e-4}{\pi\ 0.03175\ 0.45e-3} = 2.23\frac{m}{s}. \quad (16)$$

The second method to define the *Re* number is by the superficial velocity. The superficial velocity is the velocity of liquid if occupying the entire pipe and is given by: $W_{sv} = 4Q/\pi/D^2$. The *Re* number is then defined based on that velocity and the pipe diameter: $Re_{sv} = W_{sv}.D/\nu = 4Q/\pi/D/\nu \rightarrow Re_{sv} = 13{,}195$.

The flow characterization based on the Nusselt theory helps to obtain a first guess for the expected flow behavior in the drain pipe. Due to the high gravity of the liquid metals, the Re numbers are 2-3 times higher than that of water. The resulting laminar flow film thicknesses are small (thin films) because of the same reason. It is highly expected that the flows will develop unsteady turbulent patterns. Therefore, the above introduced method won't be sufficient for correct prediction of the film motion. It is possible the problem to be approached numerically by performing CFD analyses of turbulent liquid films. The CFD is superior to the simple laminar one-dimensional theory, because it can provide multidimensional solution of the turbulent liquid gas interface.

In this short introduction to vertical free falling liquid films only water experiments are briefly reviewed. One of them is [8], where tests on a 3m long (ID 32.4 mm) pipe were performed. The pipe diameter and length are almost the same as those of the DPC drain pipes. Two high resolution techniques were employed for flow characterization: PTV/PIV (particle tracking velocimetry) and PLIF (planar laser induced fluorescence). Both methods allow for accurate velocity measurements (instantaneous), gas liquid interface capturing, identification of wave appearance and propagation, and recirculation zones formation. The measurements were taken on a test section 72D from the pipe inlet. The test setup allows co-current gas to be injected in the core of the flow. The review is limited to the tests with zero gas flows. They cover a range of ReNu between 306 – 1532, which is substantially lower than the range expected during the DPC filing.

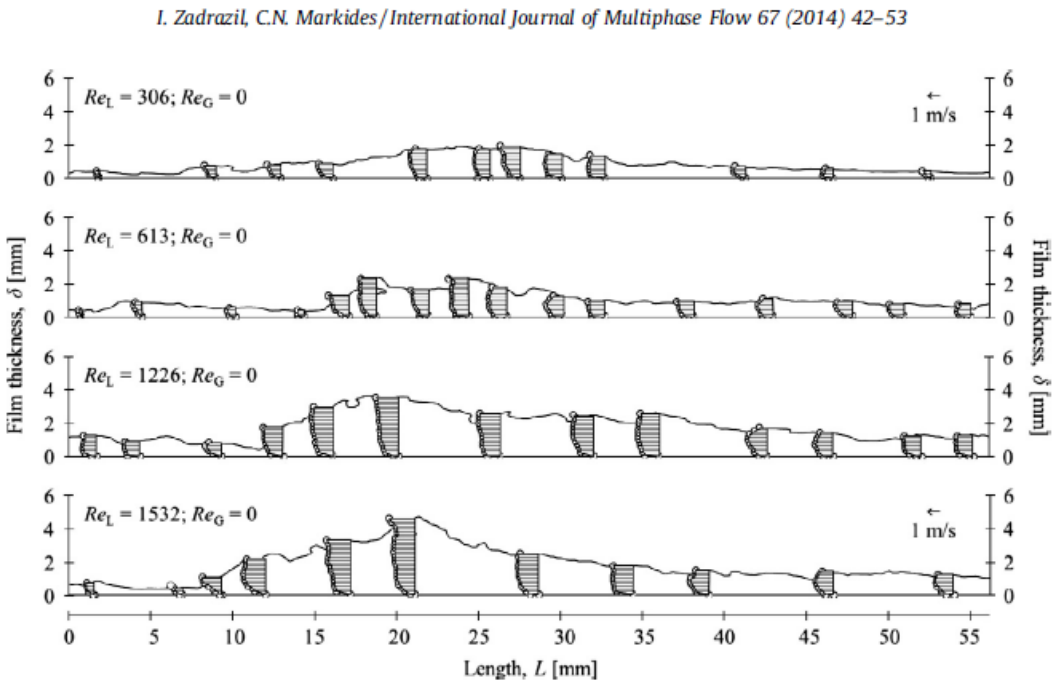

Figure 15. Liquid Film Instantaneous Velocities Showing Appearance of Waves. The Waves Grow with the *Re* Number.

A detailed image from CD-Adapco [6] shows the film thickness and the instantaneous velocities (Figure 15). For $Re_{Nu}>300$, waves start to appear and grow as the *Re* number increases. The wave velocity was also measured, which for the studied range of *Re* was around 1.5 m/s. It is noticeable that the mass transport is dominated by the wave size and not by the speed. The flow structure is defined by some basic substrate thickness (a constant thin portion of the film) and the waves traveling in this substrate. Recirculation zones are also seen in the wave crests; these are an indication of turbulent flow.

The flow visualization method used in Zadrazil and Markides [8] allowed the film velocities to be time averaged and accurately measured. Figure 16 is likely the most representative plot (also from Zadrazil and Markides) for zero gas flow, which is of interest in this study. The figure illustrates the mean film velocity profiles. The highest *Re* number results demonstrate that the film thickness stretches to 20% of the pipe's radius (~3.24 mm). These film thicknesses are in the waves. The substrate film thickness is marked with empty signs on the velocity plots. It indicates thicknesses of ~0.05R, or ~0.8 mm. Because the *Re* is about two times lower than in the case of Pb-Bi, the film's measured thickness is almost two times higher than the estimate given above for Pb-Bi. This observation points to a different flow structure that is characterized with thinner and faster films. The same conclusion is supported by comparing the profiles in Figure 16 with the estimate for the Nusselt velocity (2.23 m/s) of the Pb-Bi film. For the base film thickness (Figure 16), the velocities are between 1–1.5 m/s, and they grow slightly in the wave's crest. Apparently the time averaging does not capture the instantaneous wave velocities, which creates a perception that the waves travel with the same velocity as the film (substrate), or almost the same (~20% faster). This observation must be carefully addressed to avoid reaching a wrong conclusion. The paper by Zadrazil and Markides [8] also provides data for CFD model validation, because turbulence-related properties such as kinetic energy or Reynolds stresses are calculated from the recorded instantaneous velocity field.

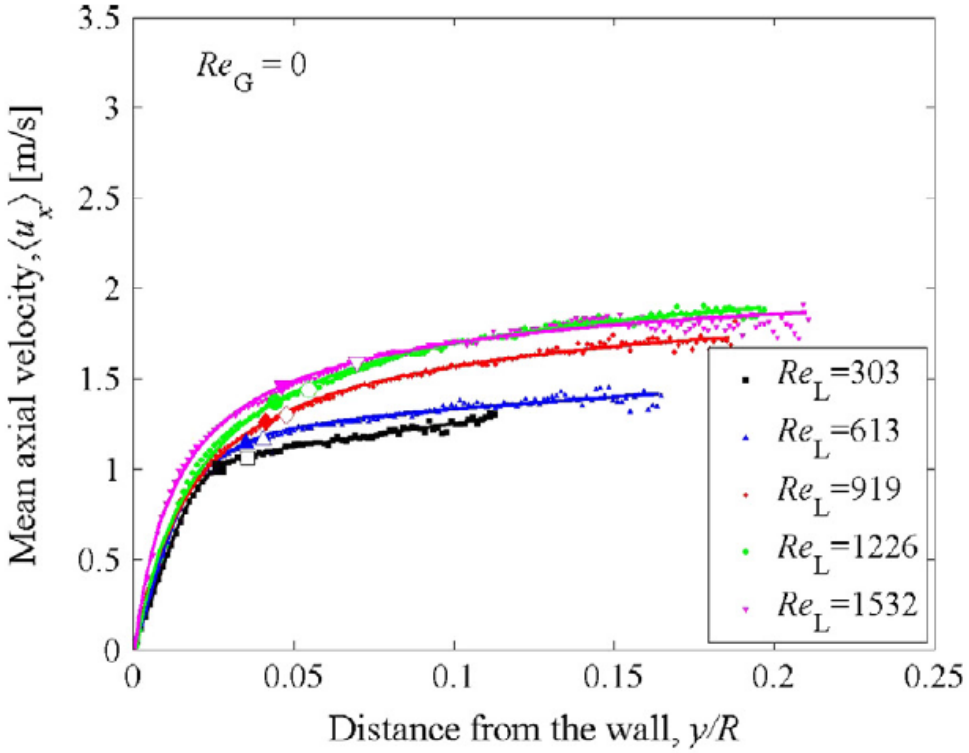

Figure 16. Axial Mean (Time Average) Velocity Profiles from Zadrazil and Markides [8] for Free-Falling Liquid Films (No Co-Current Gas Flow). The Substrate and the Average Film Thicknesses are Shown with Solid and Hollow Markers on Each Corresponding Plot.

Another interesting work is presented in Padmanaban's thesis [9]. This work did not employ such high - resolution visualization technique as used by Zadrazil and Markides [8], but the experiments were run up to higher *Re* numbers, close to or even exceeding those that are targeted in the DPC filling study. A straight vertical pipe with an ID of 1 inch (0.0254 m) and length of 4 m served as the test section. Photographs were made of the falling free films of water. The images were corrected to allow for better contrast in the wave area. Selected liquid film photos are shown in Figure 17 for three regimes with *Re* numbers of 13,348; 18,208 and 23,696. The regimes are selected to match (first one with *Re=13,348)* or to exceed the expected DPC filling *Re* numbers. The white arrows in Figure 17 indicate the region where the film flows next to the wall, to the waved area over the film, and to the gas bubbles. Annotations to the arrows provide more detail about the objects they specify.

The left image shows a liquid film with no gas, a wavy structure over the film (substrate), and a gas core with some liquid droplets. It seems that the film thickness is on the limit of beginning to disintegrate. The next image (center) has almost no gas core. The waves have grown large enough to block the entire cross section of the pipe. The flow regime starts to transition from annular film to churn-like flow in which the core is a mixture of gas and liquid. The right image demonstrates the breakup of the film and a falling flow of mixed gas and liquid. Gas is entrained in the liquid, and the liquid is entrained in the gas core. The liquid film is difficult to distinguish. This occurs at *Re* less than two times higher than the *Re* of interest in the filling analyses.

Based on this information, it can be concluded that the initially selected filling rate of 100ml/s will produce a turbulent film with large waves contributing substantially to the mass transport. The flow regime is close to a transitional mixed liquid-gas regime, which at this time is considered questionable for delivering a steady flow of liquid to the canister.

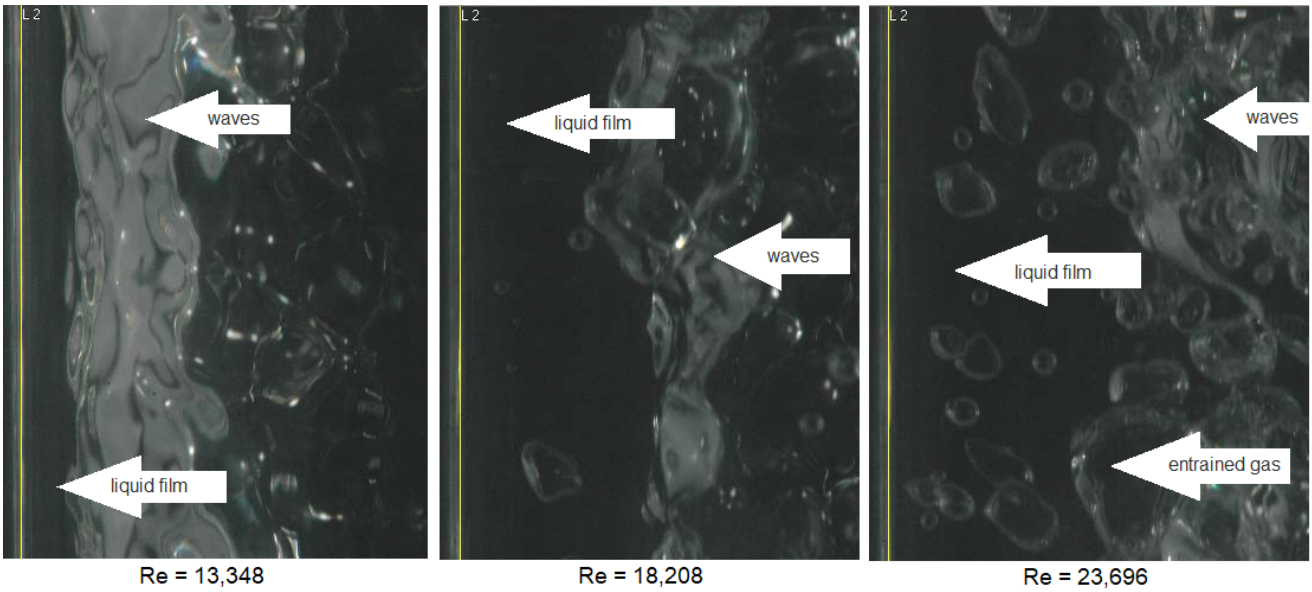

Figure 17. Photos of Free-Falling Films [9]. Only the Left Half of a Cross Sectional Area of the Pipe is Shown. The Wall is on the Far Left, and the Film is the Dark Area Next to the Wall. Gray-Colored Regions Show the Waves, and the Far-Right Image Shows the Entrained Gas.

Besides capturing the film topography, Padmanaban [9] provides measurements of the turbulent mean film thickness. The results are based on statistical processing of more than 40,000 images for each of the different flow rates. The data are correlated in analogy with the film's thickness (δ) from the Nusselt theory. To compare with other data, these data are nondimensionalized with a factor of $(\nu^2/g)^{1/3}$. The result is plotted in Figure 18. The *Re* number in Figure 18 is four times smaller than that used in this work due to different formulation (*Re = 13.195/4 = 3300).*

The nondimensional film thickness for this *Re* is *~35* (from Figure 18). Applying the factor given above, the dimensional film thickness for Pb-Bi can be calculated: *δ = 35(3.039E-14/9.81)^1/3 = 0.51 mm.*

The result is about 12% different from the Nusselt thickness of *0.45mm* given above. The difference is due to the wave formation that is captured in the experimental studies, but once averaged, it produces almost the same thickness. The average film thickness is only one of the flow characteristics. Another equally important characteristic is the wave height, which has only been measured in more recent works in which advanced visualization techniques were employed.

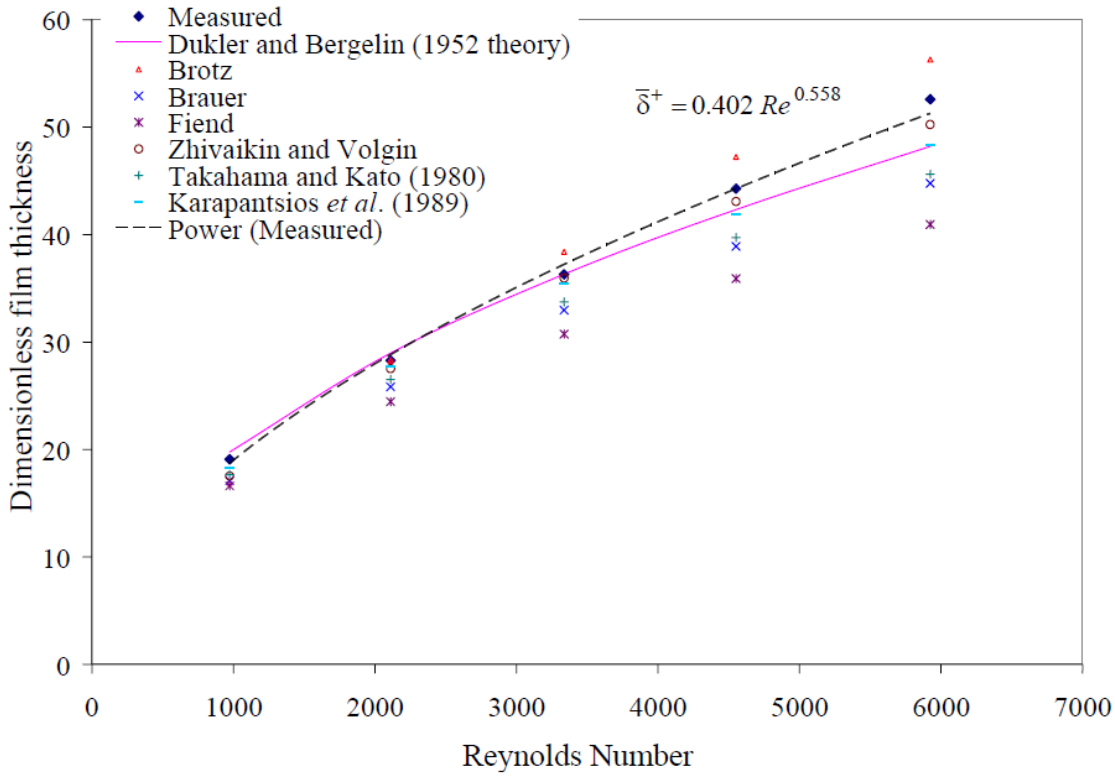

Figure 18. Dimensionless Film Thickness in Function of Re Number [9] for Comparison with Previous Experimental and Theoretical Data.

The limited review of existing data for free-falling liquid films in circular pipes reveals several useful findings.

1. There is an abundance of data for liquid films in pipes for low *Re* number flows. Data are more limited for high *Re* turbulent films because neither the theoretical models nor the experiments are easy to conduct. Most of the industrial applications involve turbulent flows, including the DPC-filling problem.
2. Within the scope of this initial work, no data were found for falling films of liquid metals. The search will continue in the future; however, it seems that experimenting with annular liquid-gas flows might be advisable in the filling demonstration project. The objective of such experimentation will prove that a steady, stable, liquid metal (Pb, Hg, Pb-Bi) film can be created and maintained for hours during the DPC filling.
3. Experimenting with liquid metals may pose new questions and may require new visualization methods, because, unlike materials most used for testing liquids, the metals are not transparent. Metals have much higher surface tension (about 6 times higher than water) than most liquids used for testing in most experiments. In the work of Kapitza [10], the surface tension is analyzed, and a parameter is introduced—$\gamma = \sigma / \rho\nu^{4/3}\, g^{1/3}$—where σ is surface tension. It is shown that the surface tension has a strong effect of the formation of waves in the film. It is expected that the liquid metal will have different film topology and perhaps different thicknesses for the same *Re* numbers.
4. Another aspect to be addressed is the drain pipe geometry and positioning in the canister. In the experiments with falling films, the pipes are well aligned and positioned perfectly vertical. In a real situation inside the canister, the drain pipe may not be vertical or even straight due to aging or other thermal or structural factors. Evaluations of the effect of pipe position and geometry on the formed liquid film might be necessary.

This initial introduction to the flow phenomena in circular pipes with free-falling liquid-gas films indicates that more studies are necessary in order to draw conclusions about using the canister drain pipe for filling with liquid metals.

2.4 Planned DPC Drain Pipe Flow Experiment

As discussed above, it is imperative to thoroughly understand the filler materials that flow through a pipe. A separate computational simulation and experiment are necessary to understand any unforeseen issue of filling a DPC using a drain pipe. This experiment will inform decision making regarding filling DPCs using a drain pipe. Due to the high specific gravity of metals, filling by creating a liquid film on the pipe walls is conceivable. The resultant flow regime is two-phase, annular. If properly organized and controlled, the filling could be smooth, continuous, without pulses, vibrations, or other hydraulic effects that may compromise the entire filling process.

The literature includes many experimental and analytical studies of vertical annular flows in pipes. However, most of these have been conducted using water or other light liquids. It is difficult to find any existing literature describing studies using liquid metals. Liquid metals differ from water in two major properties—density and surface tension—two extremely important properties when considering the annular film that develops on the pipe's wall. Experimenting with liquid metals can prove the feasibility of filling through the drain pipe. Simulations (CFD) can be carried out along with the tests to compliment the assessment and to allow for scaling the problem to a real DPC.

Most of the metals are solid at normal (room) conditions. Bringing the metals into liquid state for experimentation would be expensive. To avoid this expense, mercury can be used as a surrogate metal. Mercury is heavier than most metals and has comparable surface tension, which qualifies it as an ideal surrogate. ORNL has already developed an infrastructure for experimenting with mercury which can easily be leveraged for this type of testing.

Average liquid film thickness and topology are important for detailed understanding and simulation of annular film flow of liquid metal in vertical pipes. The existing models and correlations either have large relative errors or narrow application ranges. Therefore, a new set of experiments with mercury is being planned to provide greater understanding of the process and to complement the existing knowledge base of annular vertical pipe flows. The proposed data collection will include pressure, liquid and gas velocities, liquid film thickness, effect of viscosity, etc. Previous studies indicate that the film thickness is a function of Reynolds and Weber numbers for both liquid and gas. The collected flow regime data will be used mainly to establish limits for maximum and minimum liquid filling rates in the system. Analytical models will be developed and benchmarked along with the experiments.

2.4.1 Film Thickness Measurement Technique

Unfortunately, liquid metals are opaque and reflective, and light methods will not be applicable for flow visualization. Instead, the film's thickness can be measured using a conductivity-based technique. For a conducting liquid (e.g., mercury), the liquid film's thickness is proportional to the conductance of the film, whereas the droplet-laden gas core is not. Therefore, the approach is to impose an electrical potential between a pair of electrodes in contact with the liquid film and measure the resulting current, which is a function of the conductance of the film, hence of its thickness. This technique has been used extensively [11, 12].

A cluster of four film thickness sensors is shown in Figure 19(a). The sensor consists of one "transmitter" ring electrode, 32 "receiver" island electrodes equally spaced around the circumference, and one insulation ring. The ring and island electrodes are flush with the inner pipe wall, making the film thickness sensor nonintrusive. During the signal acquisition, the transmitter electrodes are activated successively by supplying them with a rectangular voltage pulse. For each transmitter activation, the resulting current is measured successively at the receiver electrodes in the corresponding unit. A full

cycle, which is necessary to activate all transmitters and to measure the current at all receivers, takes 0.2 ms. Therefore, the total measuring rate is 5 kHz, which is much higher than the physical phenomena observed in annular flow. The principle and the signal acquisition hardware are the same as those in the electrode-mesh sensor of Prasser et al. [13].

The sensor is calibrated experimentally using a static liquid film. It is made by inserting a nonconducting insert of known diameter into the sensor, mimicking the gas core, and filling the remaining volume between the sensor and the insert with mercury. A calibration curve is determined for each receiver with the fit-model. A typical example of a curve fit is shown in Figure 19(b). It shows that the sensitivity of the sensor decreases for increasing film thickness and that a film's thickness up to about 3.5×10^{-3} m can be measured with sufficient sensitivity.

The current measured film thickness at a receiver is a function of the film's conductance integrated over the control-volume in between the transmitter and receiver. Therefore, at each measurement location, a mean film thickness averaged over this control-volume is measured at each instant. This approach is intrinsic to the conductivity-based film thickness measurement technique and is also true for the conductivity-based measurements in the literature.

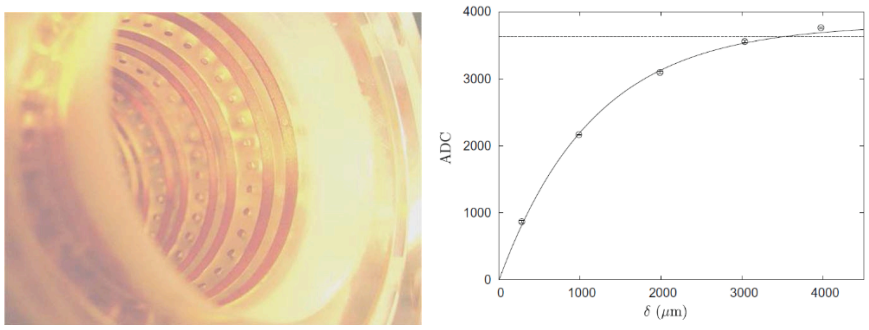

(a) (b)

Figure 19. (a) Photo of Film Thickness Sensor; Conductance is Measured between a Ring-Electrode and an Island-Electrode Flush within the Wall. (b) Typical Calibration Curve Using Stagnant Mercury Film.

2.4.2 ORNL Mercury Facility

The Target Test Facility (TTF) shown in Figure 20 is a full-scale Spallation Neutron Source (SNS)-prototypical mercury loop that was recently modified to accommodate a smaller test section using a reduced flow rate. The facility has an inventory of ~19,000 Kg of liquid mercury, and it can drive a maximum of 547 gpm using a variable frequency driver to control the loop's pump. The typical discharge shutoff pressure is 180 psig. The facility is enclosed in an isolated room that provides independent ventilation and a filter system that is able to remove mercury vapors and maintain safety levels inside the enclosure. This facility counts with mercury vapor monitors and alarms that monitor mercury vapor levels inside the enclosure and its surroundings. A team of trained personnel with extensive experience in mercury handling operates the loop.

A simple extension of the mercury loop configuration can be designed and built to experiment with a vertical pipe of the same size as the DPC drain pipe (4m, 1.25-inch ID). It will require some small modifications of the existing configuration and procurement of the necessary instrumentation. The existing data acquisition system can be used. This investment will be minimal compared to the initial investment in the existing mercury loop.

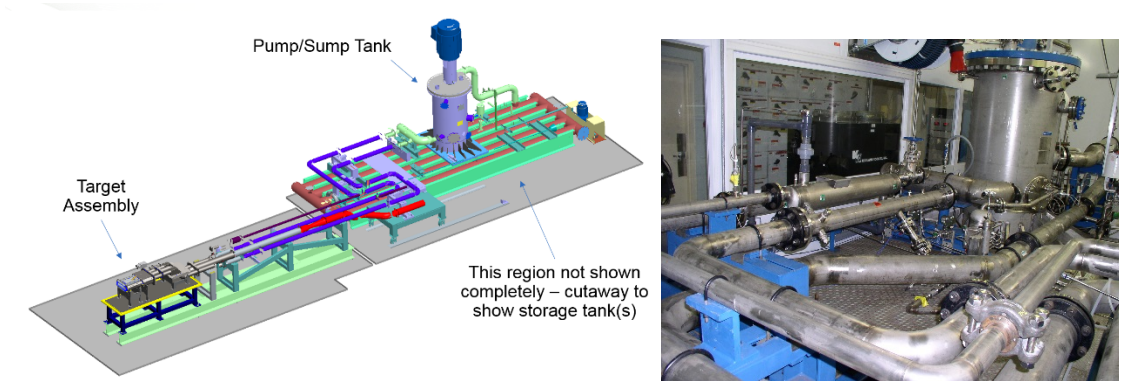

Figure 20. Target Test Facility (TTF) Mercury Loop.

2.5 Discussion

The filling simulations that have been performed on the lower region (mouse holes) of a prototypic DPC show successful filling of the inner space voids and smooth, even liquid level progression. Several liquid metals and surrogates are being tested as potential candidates for fillers. The problem requires intensive computing and is a good candidate for a high-performance computing application. Additionally, a pipe flow experiment to gain insight into filling a DPC using drain pipe has been discussed. Future work includes filling the upper regions of the canister, assessing options for filling through the drain pipe, and model validation on lab-scale experiments.

3. INITIAL FILLING DEMONSTRATION

The objective of experimental testing is to validate the computational models designed to simulate the filling process. The scope of the experimental studies documented in this report is to provide validation for single physics, or unit testing of flow simulation to determine injectability, void filling, filling time, filling method (gravity vs. pump), etc. In the subsequent phases of this work, other phenomena, such as the thermodynamic process of phase change behavior and heat transfer, will be addressed experimentally using a separate-effects approach. Ultimately, the purpose of experimental studies is to build confidence in the computational models and simulations to help ascertain the feasibility of the DPC filling process.

A separate-effects approach helps to discern the impact of complex phenomena that ultimately affect injectability and void filling due to mechanical interactions between the molten liquid and various interior surfaces of DPCs. While computational fluid dynamics (CFD) models are capable of resolving the physics of fluids, they do not include the complex physical interactions between fluids and surfaces or the intricate geometric details of DPC interiors. Typically, meso-scale effects such as surface wettability (i.e., contact angle between the fluid and the surface) and surface tension of fluids are modeled in a parametric form that defines a simple *viscous shear*. However, the stochastic variability of surfaces (such as surface roughness), and the effects of joining and intersections may have drastic impacts on the interaction between fluids and surfaces. In a physical configuration in which fluid flow is determined by a significant pressure differential, these surface effects may not be dominant. However, for this physical configuration and the planned filling process, the importance of a thorough understanding of interactions and the validation of computational models cannot be understated. Moreover, the physics of gas entrapment and void formation is not well understood.

As single-physics computational models are validated and confidence is built, a multiphysics simulation framework that couples fluid flow, thermodynamics of fluids, and heat transfer phenomena will be investigated. The multiphysics computational models and simulations will then be validated through experiments that properly address these phenomena. These models will be critical in narrowing down the

choices of candidate filling materials. This capability will also be instrumental in determining whether an external heating source will be needed, and if so, whether it will be used to design such a system. The multiphysics simulation capability may require expansion to include structural analysis. The impact of radiation hardening on mechanical properties may require additional experimental studies. Finally, identification and/or development of process instruments may be required to certify the filling process with a reasonable confidence level.

The following section presents the experimental system setup designed and built in support of the initial computational models and simulations of filling a DPC through its drain pipe. The initial experimental setup is intended to provide high-level integral data such as filling time and entrapped void fraction (determined through narrow-range level monitoring) to allow for verification and/or calibration of viscous shear parameters.

3.1 Description of the Experimental Setup

To simplify the computational models to reduce runtime and avoid numerical instabilities, spacer grids are simplified by removing detailed mechanical features. These features are fully represented in the experimental setups to guarantee that their characteristic effects are captured experimentally.

The ORNL team has decided to demonstrate the filling process in two experimental setups for initial testing. The first experimental setup mimics the computational model—with the exception of detailed mechanical features in spacer grids as stated earlier—and is intended to provide supporting data for injectability of various fluids through the drain pipe, identification of a sustainable filling rate, and resulting filling time and entrapped void space. The first setup will primarily be used for experimental demonstration of the filling process with various fluids used in the CFD simulations, as shown in Table 1.

The second experimental setup is intended to provide insight into the formation of voids in intricate geometries, such as the small and irregular spaces between the fuel rods and the springs and dimples in spacer grids. The primary focus of this setup is to provide a flexible experimentation capability while being as close to the real geometric configuration as possible. A salient feature of the second experimental setup is its modular construction and its easy disassembly. This setup will use a surrogate filler material with a low melting point, such as the paraffin wax, which melts at 64°C. This will allow for visual inspection of the filled volume, particularly to understand coalescence of multiple smaller void formations into larger voids.

3.1.1 Experimental Setup Assembly Parts

The DPC filling tests currently use scaled down models to minimize material cost and expedite the testing process while maintaining a high level of feature integrity with the actual canister design. The initial phase of testing will involve the use of liquid (water / glycerin) media to test the experimental apparatus and setup controls and to establish empirical data benchmarks for fluid dynamics simulations. The ORNL team procured three types of spacer grids from Westinghouse: (1) a 17 × 17 standard structural grid, (2) a protective (P)-grid, and (3) an intermediate flow mixer (IFM) grid. While these spacer grids are available to the team, some custom spacer grids are also being fabricated through a subcontractor to closely match the specifications [14]. The custom fabricated spacer grids will be used in the initial experiments, while the Westinghouse spacer grids will be used in later phases of the demonstration work [15].

A second experimental apparatus will also be fabricated to facilitate the use of paraffin as the filler material that can undergo phase change at a low solidification temperature. This apparatus will deviate only slightly from the liquid apparatus and will allow components of high interest to be removed and disassembled to analyze the filled space. The spacer grids for this experimental setup will be custom fabricated in a manner to allow for disassembly for post-experiment visual inspection.

The designs for each of these apparatuses are detailed below.

3.1.1.1 Liquid-Only Apparatus

The liquid-only design, as shown in Figure 21, uses polycarbonate and acrylic parts for the majority of the housing components to facilitate observations of the filling process. The canister is made from 10-inch outer diameter (OD) × ¼-inch thick acrylic tubing, and the outer basket is made from machined sheets of polycarbonate which are assembled with slot features and small fasteners. The upper and lower flanges are also made from ½-inch thick polycarbonate sheets. Two split ring flanges and 16 flanged socket head cap screws mate with a groove cut into each end of the outer container's face, compressing a gasket at each end to effectively seal the ends and prevent leakage of the liquids. A ball valve is installed near the bottom of the container to aid in draining the apparatus at the end of the experiment. The internal components are modeled as closely to the true dimensions (scaled) as possible.

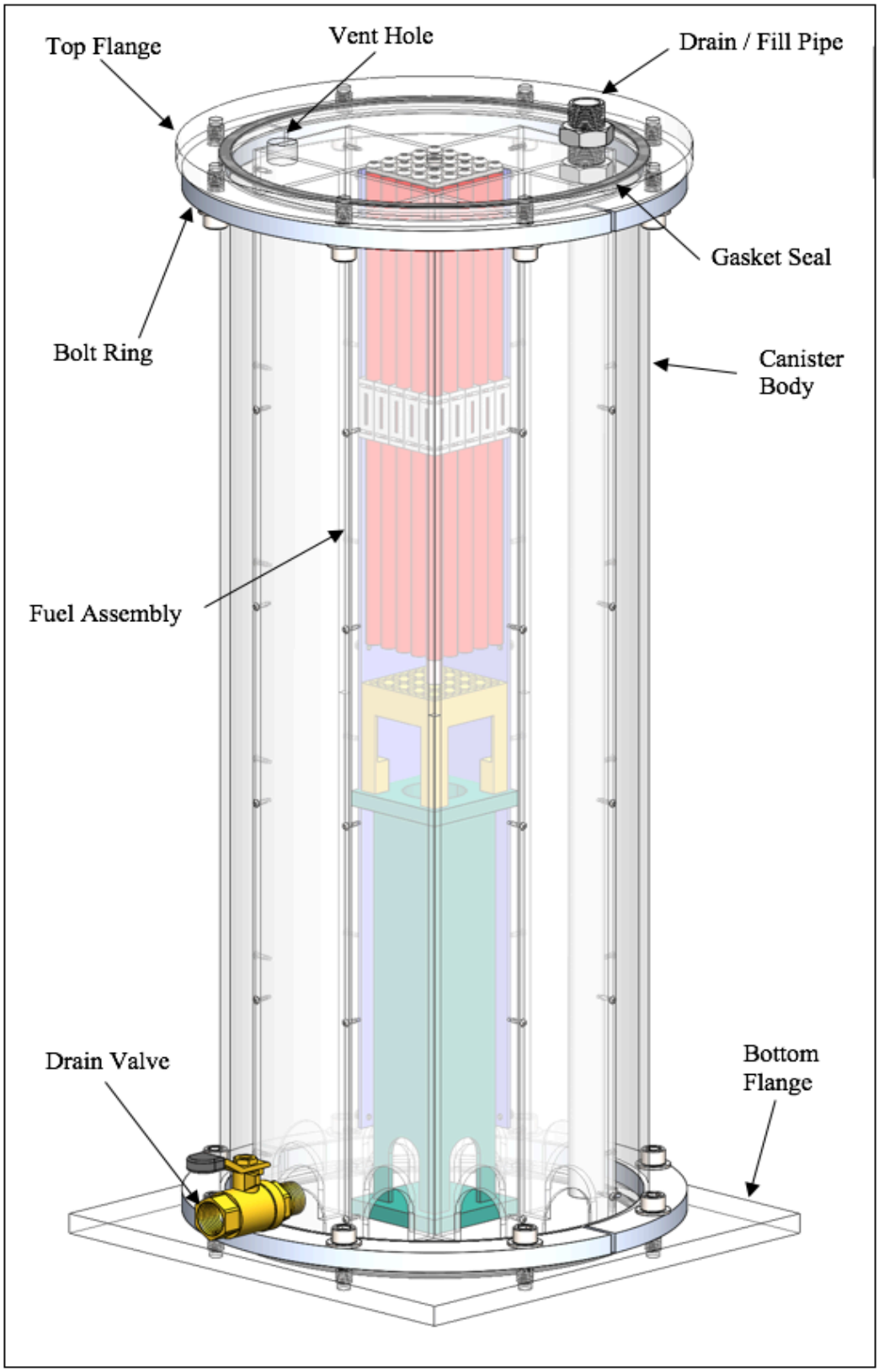

Figure 21. Polycarbonate Canister with Five-Cell Basket for Liquid Experiment.

The basket structure is the left image in Figure 22, and the bottom spacer (green), bottom nozzle (yellow), the fuel assembly (red), and the spacer grid (white), neutron absorber (gray), and the guide tube (pink) are shown as the right image in Figure 22. Figure 23 presents an artist rendering of the experimental setup.

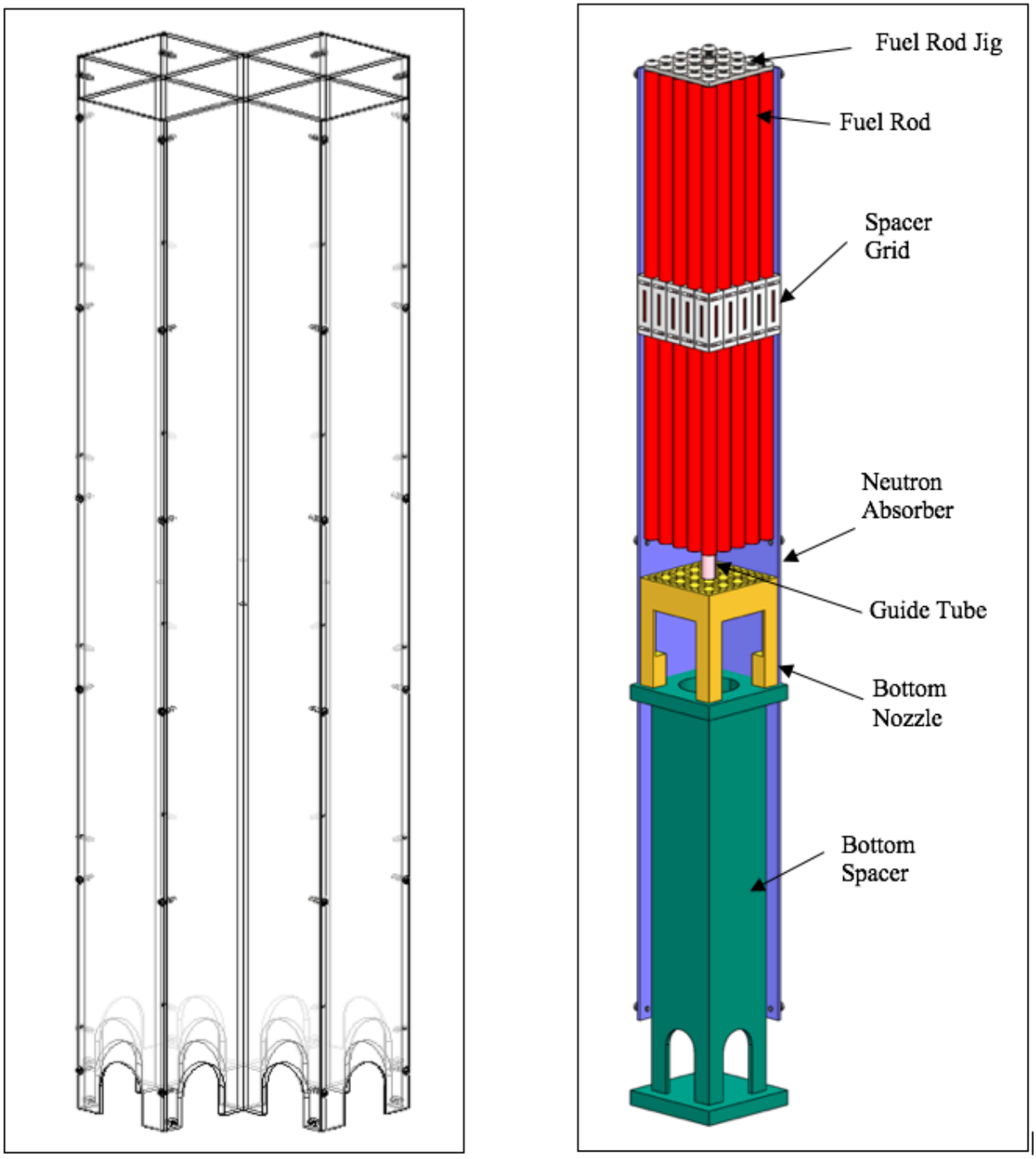

Figure 22. Polycarbonate Outer Basket (Left), and a Stack of the Fuel Assembly (Right).

Figure 23. Artist's Rendering of the Experimental Setup.

As mentioned above, ORNL received three types of spacer grids from Westinghouse. To use these grids in the experimental setup, multiple 5 × 5 grids can be created by carefully cutting the original parts. Alternatively, the original Westinghouse spacer grids can be preserved to be used in an experimental setup that uses a full-scale assembly (e.g., 17 × 17) in the later phases of the project.

Bardet et al. [14] custom fabricated a series of scaled spacer grids that closely match the original grid specifications. An example 5 × 5 spacer grid design is shown in Figure 24 and Figure 25. ORNL is collaborating with this team for fabrication of custom-made spacer grids.

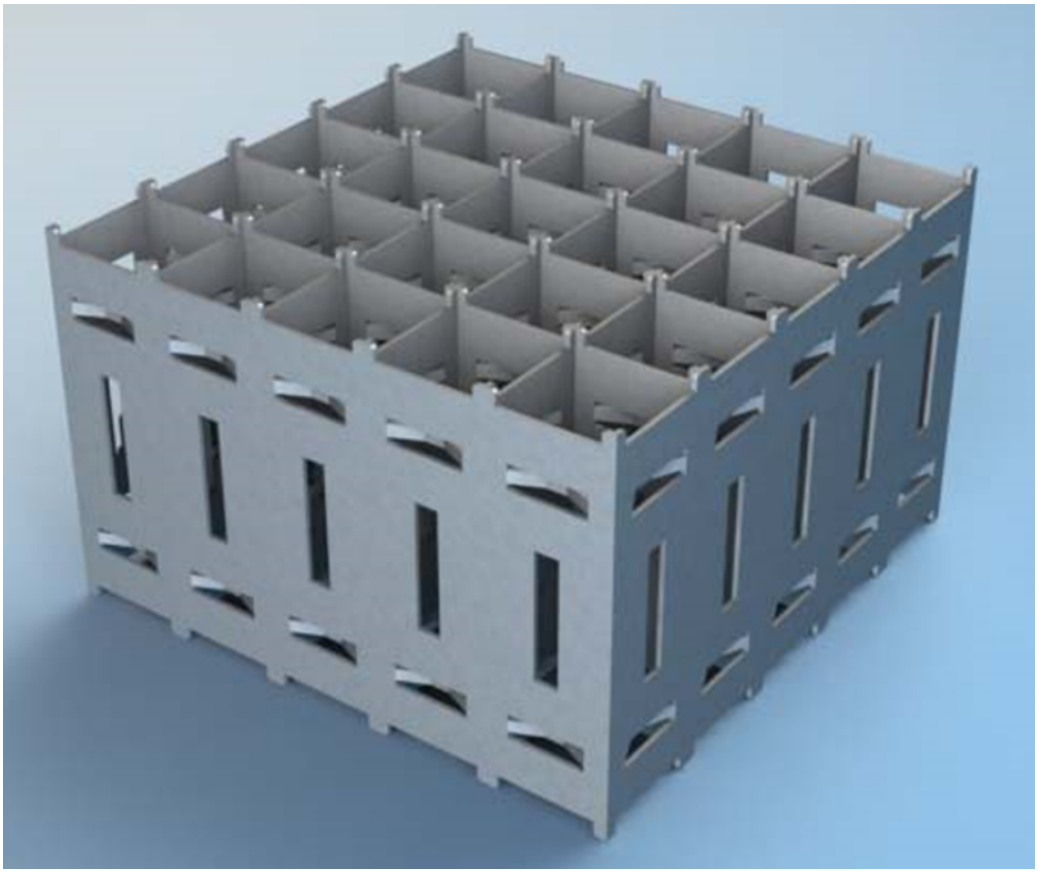

Figure 24. Side View of Spacer Grid (5 × 5) without Mixing Vanes [10].

3.1.1.2 Paraffin Filling Experiment

This design also uses polycarbonate and acrylic parts for the majority of the housing components to facilitate observation of the filling process. The container is made from 10-inch OD × ¼-inch thickness acrylic tubing which has been split into two identical halves, as shown in Figure 26. These halves are assembled using two split ring flanges and 16 flanged socket head cap screws that mate with a groove cut into each end of the outer container face. Two or more hose clamps are also used around the outer circumference to secure the canister. The edges are sealed with compressed rubber gaskets, which can be accompanied by room temperature vulcanizing (RTV) sealant if necessary. Gaskets are also located at each end of the container and are compressed by the split ring flanges. The outer basket is made from machined sheets of polycarbonate that are assembled with slot features and small fasteners. The upper and lower flanges are also made from ½-inch thick polycarbonate sheets.

The internal components are modeled as closely to the true scaled dimensions as possible, but to facilitate the disassembly of components once the paraffin has solidified, certain components have been modified.

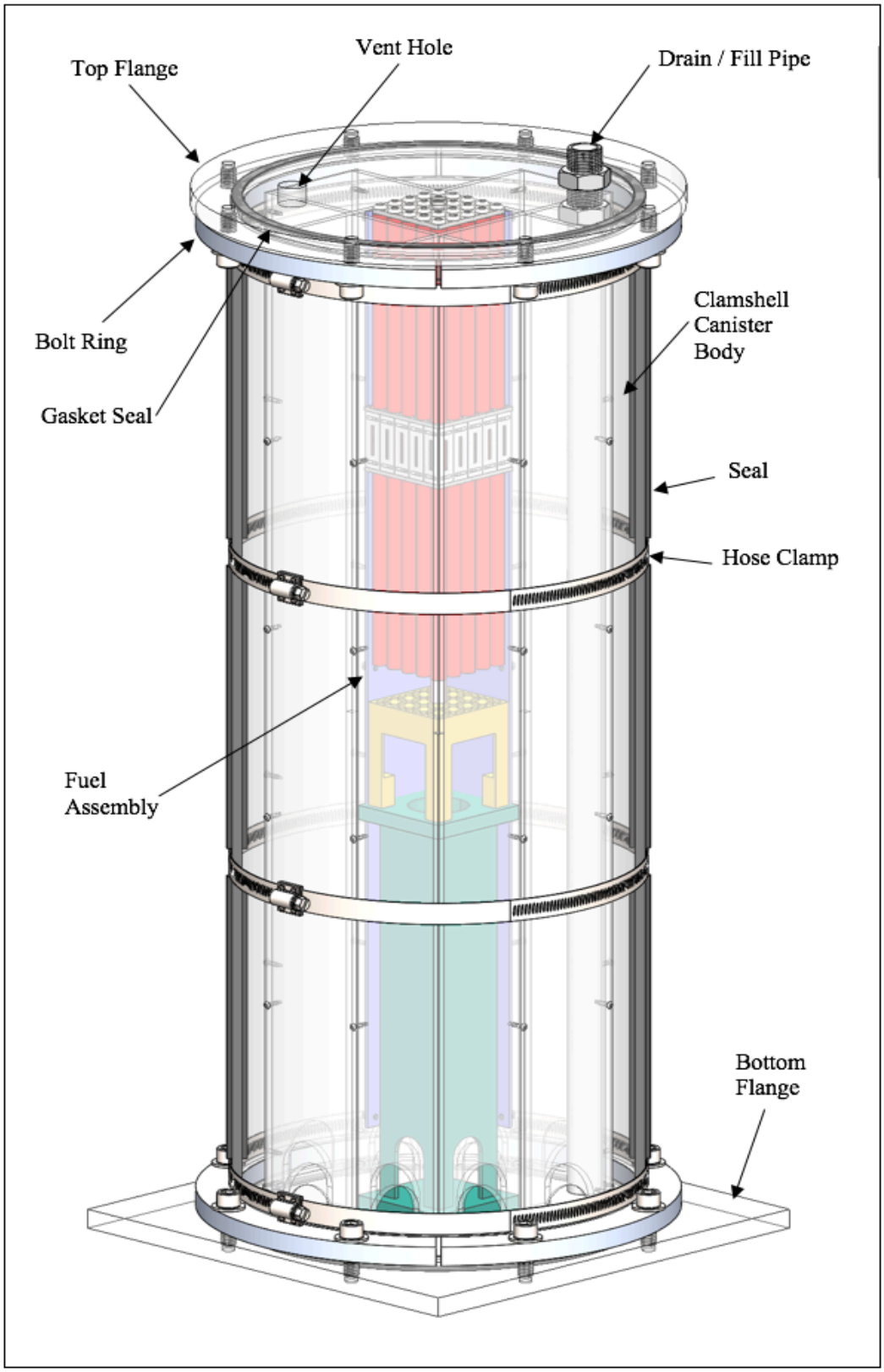

Figure 25. Polycarbonate Canister with Five-Cell Basket for Paraffin Experiment.

The grid spacer design has been modified to be easily disassembled by using upper and lower plates which contain slots to capture the grid panels. The grid panels are also modified to have tabs at each end to mate with the upper and lower plates. Figure 16 shows details of the grid panels. Figure 27 shows the exploded view of the customized modular grid assembly. The fully assembled custom grid is show in Figure 28.

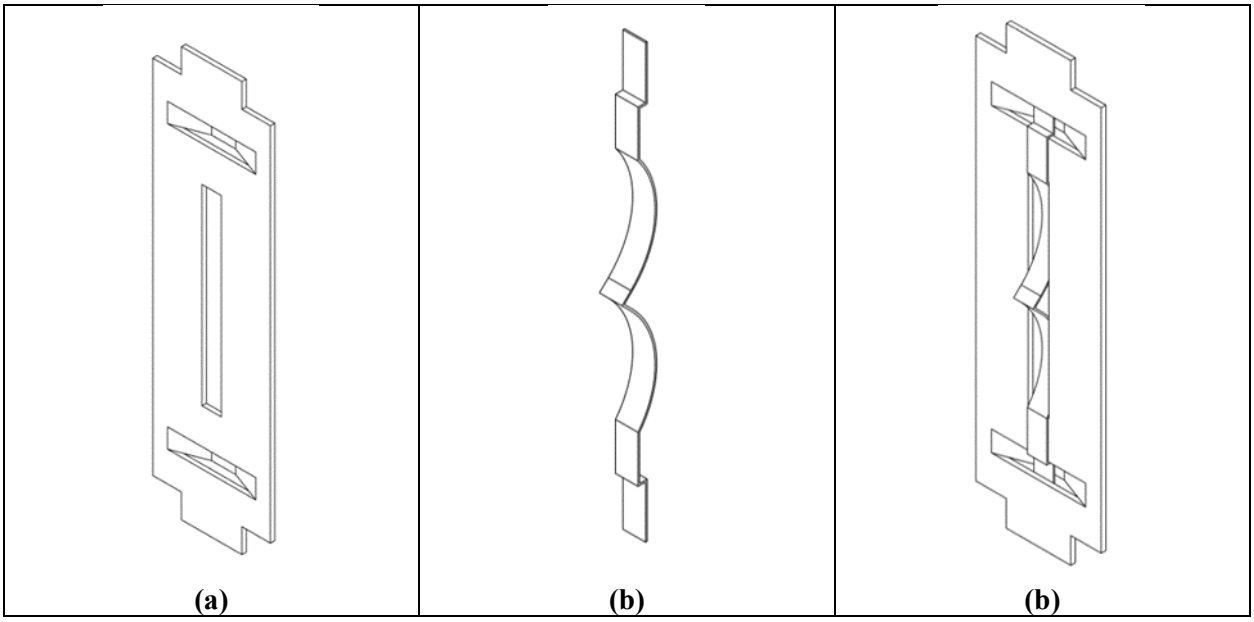

Figure 26. (a) Custom Spacer Grid with Dimple, (b) Custom Spacer Grid Compressed Spring, and (c) Custom Spacer Grid Panel with Dimple Weldment.

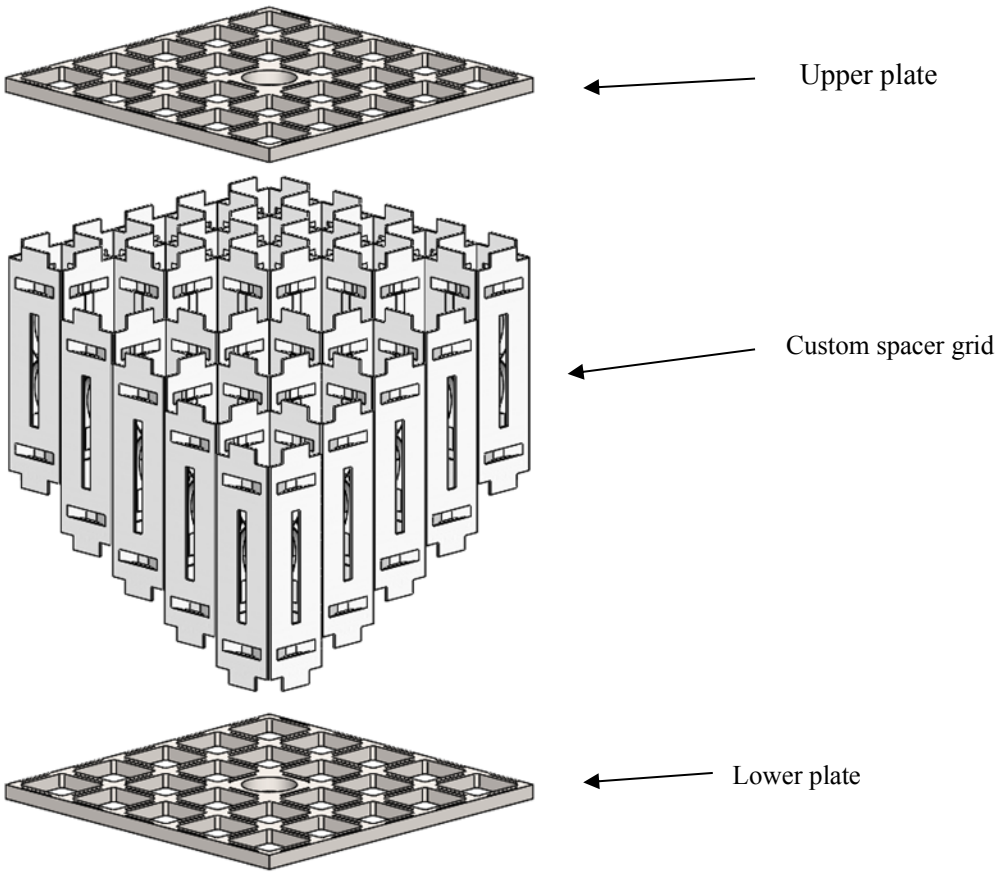

Figure 27. Exploded View of the Custom Spacer Grid Assembly

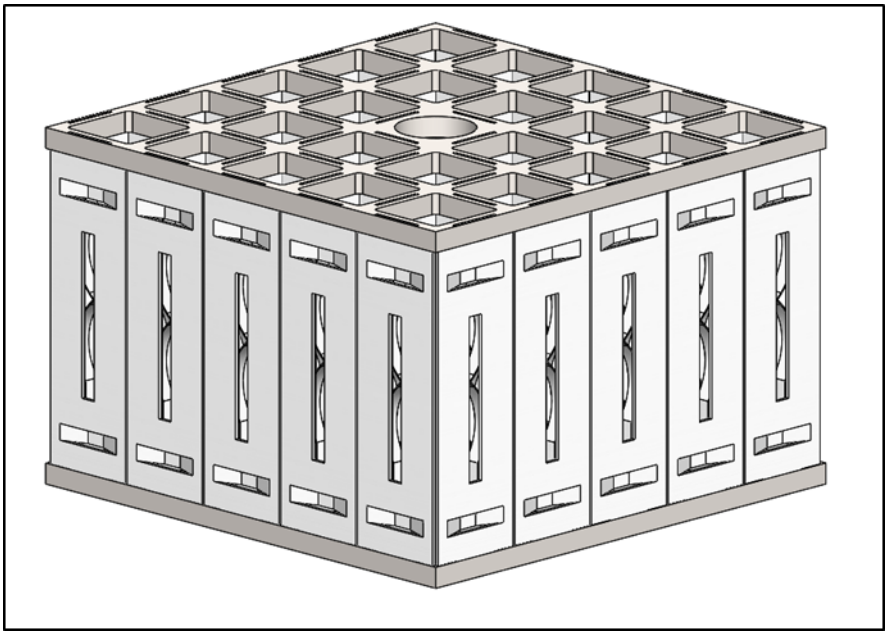

Figure 28. Fully Assembled Custom Modular Grid.

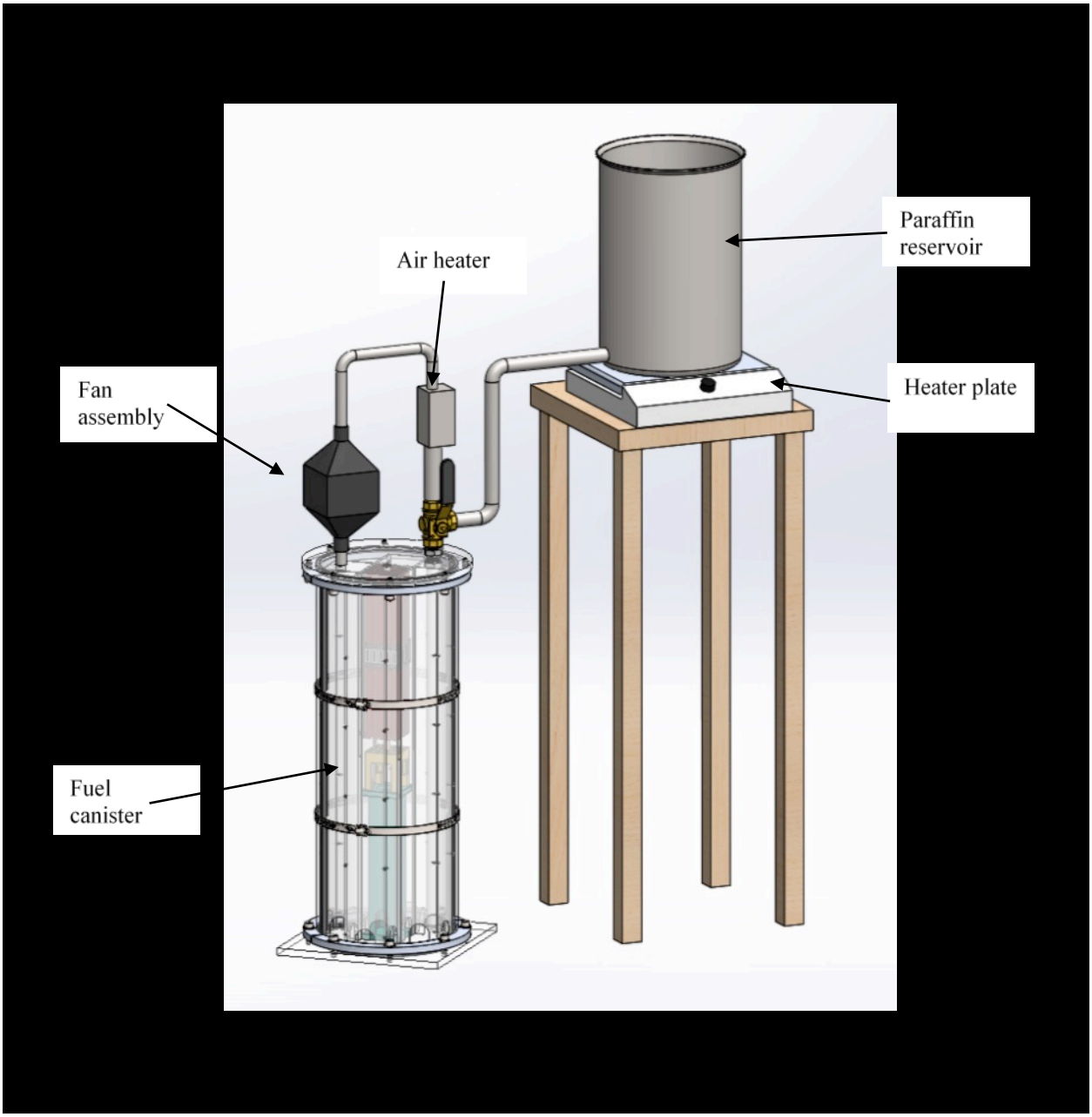

Figure 29. Set-Up for the Paraffin Experiment.

The experimental set-up shown in Figure 29 consists of a split canister assembly, an air heater, a paraffin reservoir, and a three-way valve. Initially, the three-way valve will be positioned towards the air heater tubing. The inline air heater will heat the air being circulated through the heater by the fan connected to the vent hole of the canister. A thermocouple inside the canister will register the air temperature. Once the temperature inside the canister has reached 60°C, it will be ready to be filled with paraffin. A small relief valve will also be installed on top of the upper flange to allow the air to escape as it is being displaced by the paraffin filling the canister.

Turning the three-way valve towards the paraffin reservoir will cause the paraffin to start flowing into the canister. Another valve next to the paraffin reservoir (not shown) will be used to control the paraffin flow rate. To ensure that the paraffin does not solidify before it has completely filled the canister, heat tape will be wrapped around the canister, piping, and valves. The temperature setting on the heat tape will ensure that the paraffin is maintained at 60°C. Multiple thermocouple readings will be used to ensure uniform heating during the filling experiment. Power to the heat tape, heating plate, and the air heater will have logic to ensure that components are not overheated while also ensuring that adequate temperature of the air and paraffin are maintained.

3.1.2 Experimental Setup Assembly Parts Acquisition Status

All drawings (Table 3) were finalized and forwarded to machine shops for fabrication. ORNL team is expecting to order all other parts for conducting the experiment by the end of August, 2018. Table 4 presents the parts acquisition status as of 31 August, 2018.

Table 3. Drawing part number and quantities being fabricated.

DWG	ITEM	Quantity
284-DPC-1110 (Assembly)	Panel weldment (with dimple)	25
284-DPC-1111 (Part)	Panel with dimple	37
284-DPC-1112 (Part)	Spring	37
284-DPC-1120 (Assembly)	Panel weldment (without dimple)	12
284-DPC-1121 (Part)	Panel without dimple	12

Table 4. Current (as of end of August) parts acquisition status

Item	Specification	Cost	Vendor Info	Status
Fan	1053-1116-ND	$100	Digikey	Parts received
Heater	AHPF-061	$345	Omega Engineering (Not used)	Parts received
Plate Heater (for paraffin wax)	0-300°C, hot plate	$115	3118K52, McMaster Carr	Parts received
Paraffin wax*	Nature Wax C-1	$118	General Wax and Candles	Parts received
SS-Container with temperature gauge and shut-off valve	½" NPT Connection	$218.90	10 Gal BrewBuilt Kettle	Parts received
Metal Braided Hoses	½" ID (upto 350F)	$315	McMaster Carr	Parts received
3-way, ON/OFF Valve	½" ID	$100	McMaster Carr	Parts received
High precision flow valve	¼" Tube	$380	McMaster Carr	Parts received
Flexible heating tape	½" wide	$1500	BriskHeat	Parts received
Thermocouple and reader	--	--	Already have them	--

3.2 Planned Measurements and Instrumentations Used During and After Filling

The key quantities of interest for this initial experimental work are the following:

- Flow rate of the filler material,
- Filling time, and
- Volume of entrapped gas.

The flow rate of the filler material can be measured with a high-sensitivity low-flow meter or a micro-flow meter. The filling time will be measured by a chronometer triggered by the control gate of the filler material flow controller. The volume of entrapped gas will be calculated by the level of the liquid using a narrow-range level sensor.

In the paraffin filling experimental setup, the guide tube, fuel rods, and the spacer grids will be coated with mold release for easy removal of the interior pieces in contact with paraffin. Once the apparatus is filled with liquid paraffin at temperature, the system will be allowed to cool down to its solidus temperature. After sufficient time for temperature equilibrium, the canister clam shells will be opened to expos the solid paraffin—with potential trapped gas volume. The paraffin wax will be sliced to allow access into the interior regions. Once the inner fuel assembly is accessed, the guide tube will be removed first, followed by the upper and lower plates of the spacer grid assembly. Working from the outer regions, individual spacer grid plates will be removed to expose the paraffin. The fuel rod corresponding to the area will then be pulled straight out. Sections of these regions can then be sliced using a thin knife to obtain cross sections of the paraffin to evaluate gas entrapment (void spaces). This procedure will then be repeated for all regions of the fuel assembly.

3.3 Discussion

Two initial experimental setups were designed for liquid and paraffin experiments. Data collected from these experiments will be used to validate the filling simulation described in Section 2. The paraffin experiments will require external heating like any molten metal–based fillers and will provide valuable experience to inform a full-fledged experiment using molten metal fillers. All the drawings for various initial experiment setup parts have been completed, and procurement of the parts has been initiated. ORNL has also received three spacer grids from Westinghouse. The ORNL team expects to complete the initial setup by end of FY 2018.

4. CONCLUSION

A multi-phase approach as described in the joint workplan [4] culminating to a full-scale demonstration and a fully validated multiphysics simulation/prediction capability are being pursued to support direct disposal of DPCs. An acceptable filler should establish the probability of criticality in DPCs during the disposal time frame to be below the probability threshold for inclusion in a repository performance assessment. As discussed in the introduction, the filler option to support direct disposal of DPCs is being investigated in parallel with the other options such as criticality consequence assessment. This report describes the initial single physics CFD model developed to simulate the filling process and the planned experimental setups to validate the CFD simulation. The initial filling simulations of the lower region (mouse holes) of a prototypic DPC show successful removal of the inner space voids and smooth (even) liquid level progression. The filling through the drain pipe is currently being investigated as a decoupled process due to complexity of modeling flow in a narrow long pipe. A flow experiment through a pipe to understand any issue related to filling a DPC using drain pipe is also discussed in this report.
Additionally, the initial experimental setups have been designed, and the various assembly parts are being procured.

5. REFERENCES

1. StoreFuel and Decommissioning Report, Ux Consulting Company, LLC ("UxC"), Vol. 20, No. 238, June 2018.
2. E. Hardin et al., *Investigation of Dual-Purpose Canister Direct Disposal Feasibility (FY14)*, FCRD-UFD-2014-000069 Rev.1, October 2014.
3. J. B. Clarity, K. Banerjee, H. K. Liljenfeldt, and W. J. Marshall, "As-Loaded Criticality Margin Assessment of Dual-Purpose Canisters Using UNF-ST&DARDS," *Nuclear Technology*, 199(3), 245–275 (2017).
4. *Joint Workplan on Filler Investigations for DPCs*, Sandia National Laboratory, SFWD-SFWST-2018-000481, Rev.0, December 2017.
5. Holtec International, *Final Safety Analyses Report for the HI-STORM 100 Cask System*, 2010.
6. CD-Adapco, *STAR-CCM+ 13.02 Theory Guide*, 2015.
7. https://mdx.plm.automation.siemens.com/star-ccm-plus.
8. I. Zadrazil and C. Markides, "An experimental characterization of liquid films in downwards co-current gas-liquid annular flow by particle image and tracking velocimetry," *Int. J. of Multiphase Flow* 67, 2014.
9. A. Padmanaban, *Film Thickness Measurements in Falling Annular Films*, Thesis McS, University of Saskatchewan, 2006.
10. P. Kapitza, Wave flow of thin layers of a viscous fluid, Collected papers of Kapitza, Pergamon Press, 1965.
11. S. V. Paras and A. J. Karabelas, "Properties of the liquid layer in horizontal annular flow," *Int. J. Multiphase Flow* 17 (4), 439–454 (1991).
12. L. B. Fore and A. E. Dukler, "Droplet deposition and momentum transfer in annular flow," *AIChE J.* 41 (9), 2040–2046 (1995).
13. H. M. Prasser, A. Boettger, and J. Zschau, "A new electrode-mesh tomograph for gas–liquid flows," *Flow Measure. Instrum*. 9, 111–119 (1998).
14. N. A. Weichselbaum et al., *Surrogate Spacer Grid Design for Fluid-Structure Interactions Studies in Fuel Bundles*, The George Washington University, Washington, DC.
15. A. Rubin et al., *Volume I: Experimental Database and Final Problem Specification, OECD/NRC Benchmark Based on NUPEC PWR Subchannel and Bundle Tests (PSBT)*, November 2010.